

Department of Precision and Microsystems Engineering

Parametric study of an elastic singularity-based frequency doubler for concatenation

Luuk Samuels

Report no	:	2023.015
Coach	:	Dr. ir. D. (Davood) Farhadi
Professor	:	Dr. ir. D. (Davood) Farhadi
Specialisation	:	Mechatronic System Design (MSD)
Report type	:	Thesis report
Date	:	3-03-2023

Preface

The setup of this paper is based on the requirements set by Science for publication. This includes that the materials and methods section is included in the supplemental material. This also means that the paper is focused on results while for any other important details the supplemental material is referenced.

Parametric study of an elastic singularity-based frequency doubler for concatenation

by

L.E.A.M. Samuels

to obtain the degree of Master of Science
at the Delft University of Technology,
to be defended publicly on Friday March 3, 2023 at 14:30

Student number: 4730003
Project duration: September 14, 2021 – March 3, 2023
Thesis committee: Dr. ir. D. (Davood) Farhadi, TU Delft, supervisor
Prof. dr. ir. JL (Just) Herder, TU Delft, chair
Dr. ir. S. (Sid) Kumar, TU Delft



Abstract

The use of elastic frequency multipliers presents the ideal platform to address the coupling between the footprint and range of motion of elastic mechanisms. By transmitting unidirectional into reciprocating motion they efficiently increase the range of motion without a huge compromise in size. In this thesis, an elastic frequency doubler based on an eight-bar mechanism that exploits the displacement around a singularity to double the frequency is presented. Higher frequency multiplications can be achieved by concatenating this mechanism, surpassing previous designs in the literature. To facilitate effective concatenation, criteria for optimization were established and a design study was conducted to determine the optimal geometrical parameters of the mechanism. The utilization of not only the actuation capabilities but simultaneously leveraging the inherently stored strain energy during operation has the potential to serve as the foundation for a novel group of architected materials. The embodiment of both functionalities makes these architected materials highly desirable for control in autonomous robots where, through the exploitation of close synergy and decrease in dissipation, this multifunctionality could increase the efficiency in usage of the usually limited space and available energy.

Introduction

The quest for efficient actuation and energy storage methods has led to the use of elastic mechanisms with programmable outputs. These mechanisms simultaneously embody both functions by harnessing the elastic energy stored in their deformed slender beams. This approach offers some significant benefits such as a monolithic design, more efficient energy utilization, and a close synergy between the functionalities of energy storage and actuation [1]. In this paper, such an elastic mechanism with programmable output will be presented and investigated. The ability to realize a desired mechanical response and the compliance of the mechanism are highly desirable for applications such as the actuation and storage of energy in soft robotics, where these mechanisms could achieve more efficient usage of the already limited space and energy and enable the creation of more capable machines while reducing their mechanical complexity [2, 3, 4, 5, 6, 7]. Or for innovation in mechanical watch design, where the increase in energy and space efficiency due to the monolithic multifunctionality could be exploited [8]. Additionally, the absence of rigid body contact in elastic mechanisms increases their energy efficiency, and life span and decreases the need for maintenance, making them ideal for longevity-promoting low-maintenance environments where energy is often limited such as untethered soft robotics, minimally invasive surgery, the high-tech semiconductor industry, or outer space applications.

It has recently been shown that the fundamental limitation in the range of motion of elastic mechanisms can be overcome through the use of frequency multiplication transmissions [9, 10, 11, 12, 13, 14, 15]. As elastic mechanisms do not allow for infinite continuous rotation, their range of motion (ROM) is fully dependent on the footprint of the mechanism. This limitation is eliminated by instead transmitting unidirectional into reciprocating motion; i.e. frequency multiplication. For mechanisms where the displacement is of equal amplitude a higher frequency is preferred as this increases the ROM.

Recent developments in the field of elastic frequency multipliers are however only limited to the fabrication and testing of a handful of elastic frequency dou-

blers and a single successful concatenation to achieve a frequency quadrupler, while higher frequencies have only been conceptualized. This is attributed to, among other challenges, the difficulty in concatenating these devices to exponentially higher frequencies, due to the desired input-output relations and the limited load capacity of the frequency multiplier building block being unable to handle the increase in actuation stiffness upon concatenation. Additionally, establishing criteria to allow for efficient concatenation has yet to be explored.

The main working principles of elastic frequency multipliers in literature, as described in [16], can be classified into four categories. Firstly, the singularity-based multipliers [14, 15], which involve moving a mechanism around a singularity point to double the frequency. Secondly, the contact-based multipliers [9], that rely on altering the boundary conditions through mid-operation contact with the outside. Thirdly, the tensioned beam multipliers [13], that employ the tensioning and untensioning of beams to change the boundary conditions mid-operation. And lastly, metamaterial-based frequency multipliers [11, 12], where transition waves are guided through the material by either changing the wave-velocity intercellularly or by adding defects to create a reciprocating motion.

Inspired by the recent advancements in elastic frequency multipliers, this study explores a wide design space of parameters for an eight bar based elastic frequency doubler building block that leverages displacement around a singularity to double the frequency, in order to achieve efficient concatenation.

In this paper, we first demonstrate that geometry plays a critical role in determining the qualitative and quantitative behavior of the frequency doubler and that by tuning the geometric variables, the performance can be improved. After this, to facilitate efficient concatenation of the device, we established criteria and performed a wide parameter sweep to identify the optimal geometric parameters. The result of this research has the potential to form the basis of new actuation methods for untethered soft robotics in low-maintenance fields or harsh environments. And is a big step toward embodying both actuation and storage of strain energy into a single monolithic architected material.

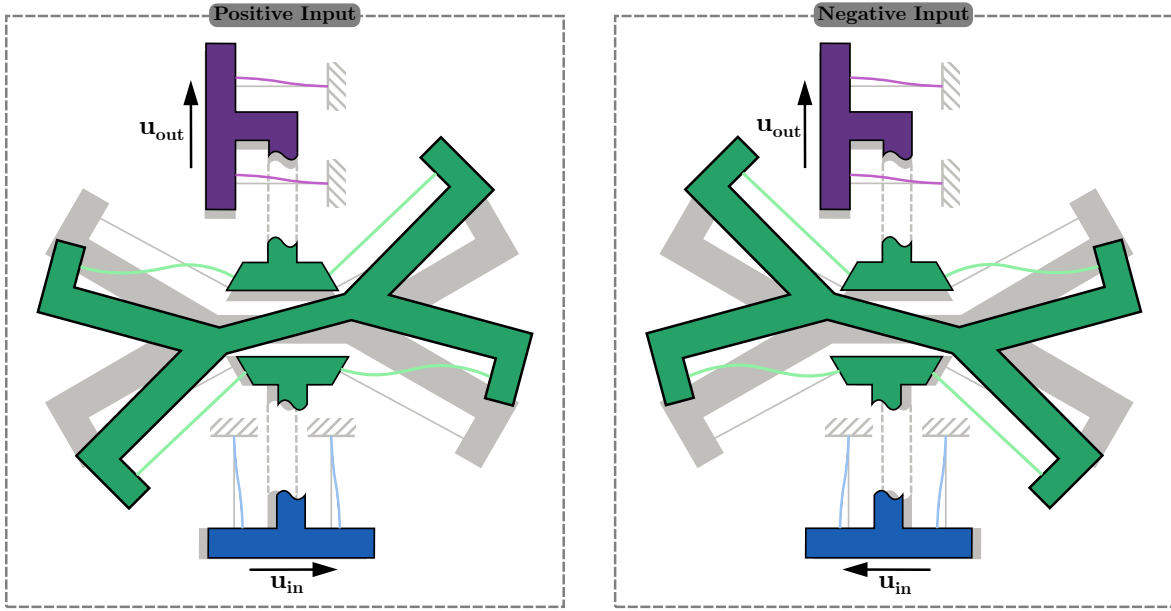


Fig. 1: Deformation of the frequency doubler. Input-output displacement characteristics of the eight-bar mechanism based frequency doubler building block for a positive input displacement (left) and a negative input displacement (right).

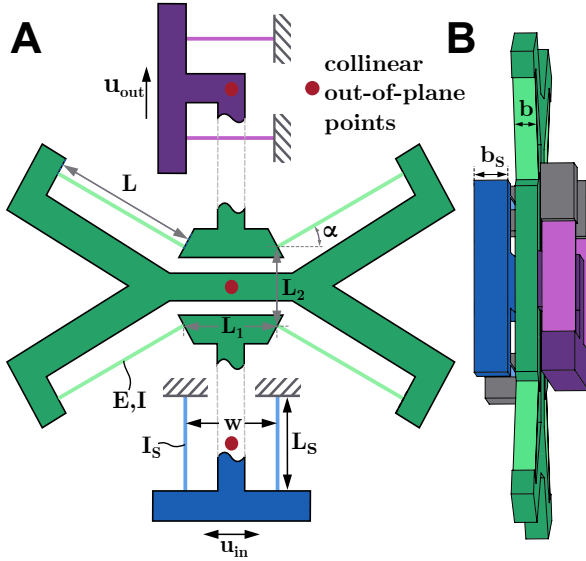


Fig. 2: Important Parameters of the frequency doubler. (A) Schematic of the planes of the eight-bar-mechanism based frequency doubler building block. (B) Top view showing the mechanisms multiplanarity.

Results & Discussion

Exploiting the singularity

To create a frequency doubling building block that allows for concatenation we explored the behavior of an eight-bar-mechanism based frequency doubler (see Fig. 2). It exploits the movement around a singularity point in the design, making the output shuttle strictly move upwards independent of the direction of the input (as depicted in Fig. 1). The singularity occurs due to the nondeterministic reverse kinematics present for the equilibrium position of the mechanism. This specific design was chosen as it has a good number of tunable variables. The proposed mechanism consists of three parts: the input shuttle (blue) and output shuttle (purple) with thickness (b_s), which function as linear guides

ances, and the butterfly mechanism (green) with thickness (b). Furthermore, the length between the shuttle's flexures is indicated with (w) and their length with (L_s). To decrease working volume and facilitate easier concatenation the mechanism is made out-of-plane (see Fig. 2 B). This is done in such a way that the center of the three parts are collinear out-of-plane points for a line that is orthogonal to the main plane (see Fig. 2 A). Additionally, this chosen construction also minimizes the resulting moment on the output, by a force on the input, by limiting the moment arm.

To investigate the response of the frequency doubler mechanism finite element analyses (FEA) were conducted for different combinations of the angle, α , normalized length of the butterfly flexures $l = L/u_{in}$ and the normalized horizontal and vertical distance between the butterfly flexures, $l_1 = L_1/u_{in}$ and $l_2 = L_2/u_{in}$ respectively (see Fig. 2), where u_{in} is the maximum displacement of the input shuttle. In the simulations (which were conducted in the enterprise version of 2021R2 Ansys Mechanical APDL) the flexures were modeled as BEAM188 elements based on the Timoshenko beam theory while the rigid bodies were modeled as MPC184 elements assumed as fully rigid due to their relatively large stiffness. Additionally, it uses a linear isotropic material type with Poisson's ratio $\nu = 0.4$, Young's modulus $E = 1700 \text{ MPa}$, yield strength $\sigma_y = 48 \text{ MPa}$, and square cross sections with area moment of inertia $I = 4.86 \times 10^{-13} \text{ m}^4$ for the butterfly flexures and $I_s = 7.29 \times 10^{-13} \text{ m}^4$ for the shuttle flexures (See supplementary material for more details on the setup of the simulations).

Influence of design parameters

Having determined the frequency doubling capabilities of the chosen mechanism, we then started investigating if and how changing the earlier defined parameters influences the behavior of the mechanism. This was done by changing some of the variables while looking

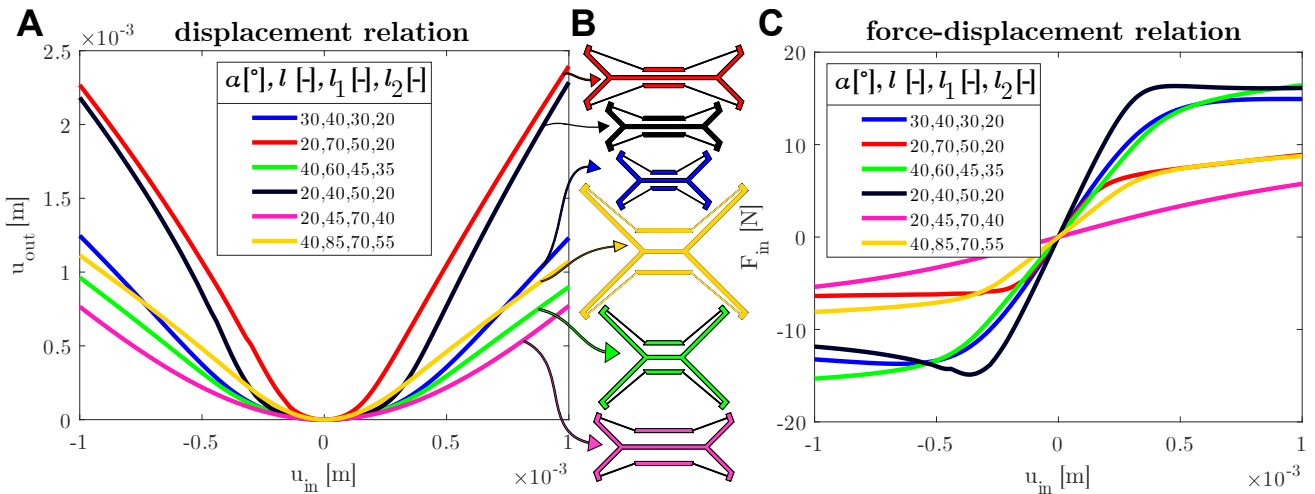


Fig. 3: Geometry and behavior for a handful of designs. (A) Input-output displacement graph showing frequency doubling capabilities and the influence of the geometry. (B) Schematics of the designs showing the geometry and size differences. (C) Force-displacement graph indicating the influence of geometry on the input stiffness behavior of the designs.

at the displacement transmission (input to output displacement) and the force-displacement relation at the input (see Fig. 3), for changes in behavior. Examining the displacement relation plot (Fig. 3 A), it is evident that changing the parameters within the here specified bounds does not restrict the frequency doubling capabilities that are inherent in each design. However, it can be observed that the geometrical advantage (*G.A.*), which is the relation of the output versus input displacement, nearly quadruples between the designs. And, that each of the designs has a qualitatively different response to the given input. This difference becomes even more evident when observing the force-displacement relation (Fig. 3 C). While one of the designs has an almost linear relation for the whole domain others show only linearity for a smaller domain near the origin. Additionally, it can also be noticed that a transition area is present after which increasing the input displacement causes the stiffness to drop rapidly. For most of the designs, this stiffness stays nonzero and positive, however, some show an almost zero-stiffness behavior while for a single design buckling behavior can even be discerned. The results of our analysis, shown in the plots, demonstrate that modifications in the parameters significantly affect the mechanism's response, and highlight the strong interdependence between the variables.

Establishing criteria for effective concatenation

Having demonstrated that the interdepending geometry of the mechanism has a significant impact on its response, both qualitatively and quantitatively, we proceeded by investigating the desired behavior with concatenation in mind and used this to establish criteria. Three independent criteria were established as the cornerstones for effective concatenation. First of all, the output displacement should be twice that of the input ($G.A. \approx 2$). As in this case, the amplitude of the input and output signal are similar, meaning when concatenated exactly the same motion domain the mechanism is designed for is used. The second criterion is sinusoidality, which is a qualitative analysis of whether a

sinusoidal input gives a sinusoidal output with twice the frequency. Sinusoidality was selected instead of the criterion of linearity, exclusively found in literature, for several reasons. One reason is that a linear response from input to output is impossible due to the infinite acceleration occurring near the singularity point. Another reason is that a linear input in the form of a triangular wave consists of a lot of high-frequency vibrations which could cause unwanted resonance in the mechanism or its application. Furthermore, similar to the first reason, a triangular input or output will always be just an approximation due to the impossible infinite acceleration required. In order to achieve a perfect sinusoidal input-output relation the displacement relation has to follow a hyperbolic cosine function (see Supplementary material for more details).

The first two criteria are both fully dependent on the kinematics of the mechanism, however, as the mechanism is essentially a transmission it is also important to look at the influence of a load on the output. This will be done with the third criterion, which is the load capacity of the mechanism and essentially establishes the load it can handle until a certain deviation in kinematics is reached. In this case, the deviation was set to 1%.

In pursuit of identifying the optimal mechanism for the established criteria, the emphasis will be placed on selecting a device that produces a good *G.A.* as this criterion has the biggest impact on concatenability out of the three. Additionally, to make sure the yield strength of the mechanism is not surpassed during operation a limit on the maximum stress with a safety factor of 1.5 is set (see Supplementary material for more details on the setup of criteria).

Improving the frequency doubler's response

Up to this point, we have demonstrated that the geometry of the design strongly influences the response of the frequency doubler and have determined the necessary criteria for concatenation. Driven by these results, we continued by setting up the design space systematically

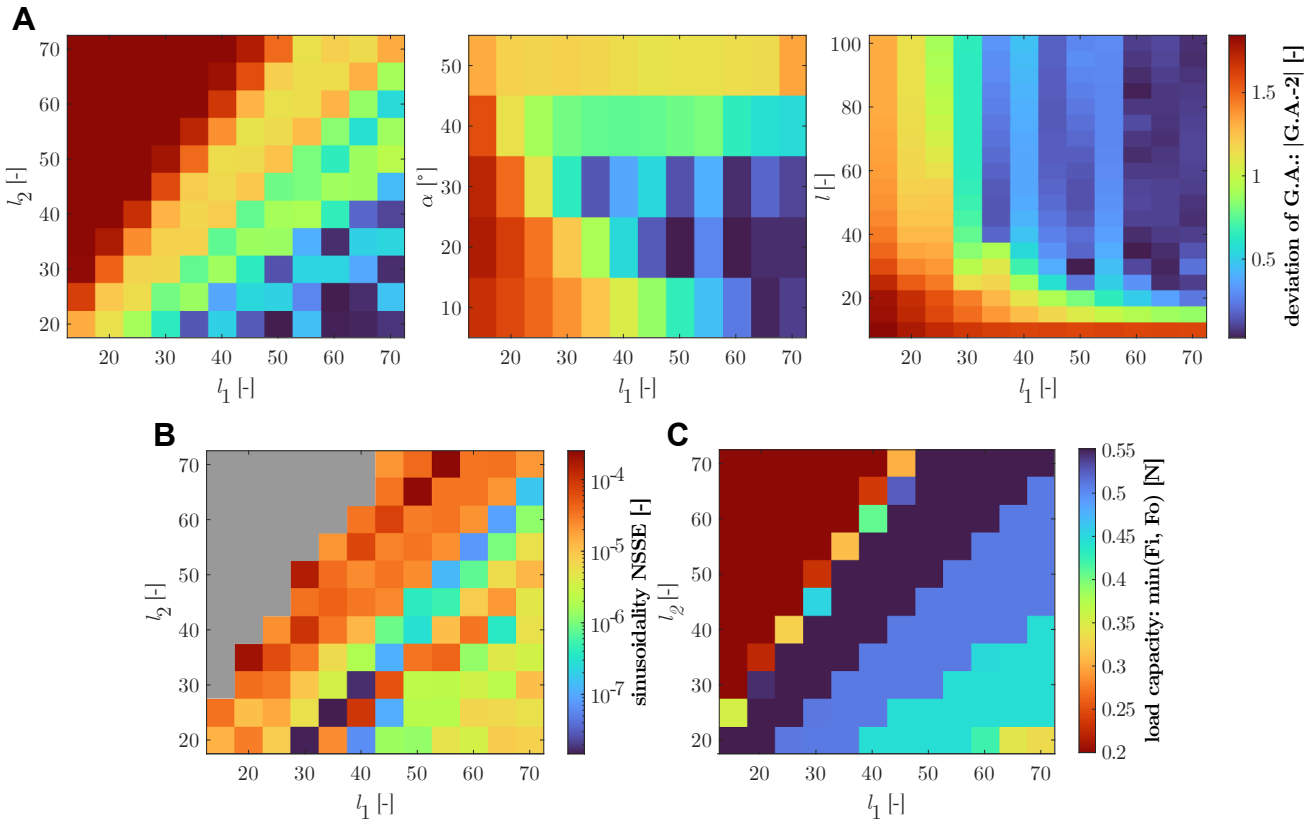


Fig. 4: Mechanical response of the frequency doubler for the preliminary investigation. (A) Evolution of the deviation of the geometrical advantage, $|(\text{G.A.}) - 2|$, as a function of the normalized horizontal distance between the butterfly flexures, l_1 and (left) the normalized vertical distance between the butterfly flexures, l_2 , (middle) the angle of the butterfly flexures α , and (right) the normalized butterfly flexure length, l . (B) Evolution of the sinusoidal normalized sum of square error, Sinusoidal NSSE, as a function of the normalized horizontal distance between the butterfly flexures, l_1 , and the normalized vertical distance between the butterfly flexures, l_2 . The grey area consists of points where the $\text{G.A.} < 0.2$, for which the sinusoidality was not evaluated. (C) Evolution of the load capacity, minimum of input force with output constrained and output force with input constrained for 1% of the input displacement, as a function of the normalized horizontal distance between the butterfly flexures, l_1 , and the normalized vertical distance between the butterfly flexures, l_2 .

with features such as manufacturability, compliance, functionality, and footprint in mind to improve the performance of the frequency doubler. Due to the high-computational cost the resulting wide design space (i.e. $10^\circ \leq \alpha \leq 50^\circ$, $10 \leq l \leq 100$, $15 \leq l_1 \leq 70$ and $20 \leq l_2 \leq 70$) was initially explored with a preliminary investigation of 12,500 design combinations.

In terms of geometrical advantage (G.A.) (see Fig. 4 A), it is evident that for smaller values of the horizontal spacing between the flexures (i.e. $l_1 < 35$) and flexure length (i.e. $l < 20$), and larger values of the angle (i.e. $\alpha > 30$) the G.A. does not meet the necessary requirements. Furthermore, an examination of the relationship between the horizontal (l_1) and vertical (l_2) spacing between the flexures reveals that the optimal value of the G.A. is obtained when the horizontal distance is relatively larger (i.e. $l_1 > l_2$). Intuitively this relation is not surprising as a longer input rotation arm compared to the output is required in order to achieve doubling of the input displacement. Similarly, using the same logic, increasing the angle α also decreases the ratio l_1/l_2 needed (see Fig. S15), of which the result can be observed in Fig. 4 A.

Additionally, a clear correlation between the horizontal and vertical spacing is again observable when inspecting the other criteria (Fig. 4 B-C). And, while for load

capacity a more equal value for the length is optimal (i.e. $l_1 \approx l_2$) as it reduces the discrepancy between the horizontal input and vertical output load capacity resulting in a higher minimum value, the G.A. and sinusoidality are improved as previously discussed when the horizontal spacing is relatively larger.

Furthermore, analysis of the other parameters for the sinusoidality and load capacity (see Fig. S14), shows that although performance in terms of sinusoidality and load capacity improves with higher values of α , it will ultimately be limited by the worsening of the G.A. for these values. This correlation between the increased load capacity and α can be understood by recognizing that for smaller angles the nearly horizontal flexures do not effectively resist output loads, jeopardizing the load capacity. Meanwhile, for the flexure length (l), which has almost no influence on the deviation of the G.A. as long as $l \geq 20$, a compromise between the sinusoidality that improves with increasing l and the load capacity which worsens with increasing l , as a result of decreased stiffness, will have to be made.

Accompanied by these findings, we were able to narrow down the design space to the more promising areas, to allow us to conduct a more thorough search. In this refined design region (i.e. $10^\circ \leq \alpha \leq 36^\circ$, $30 \leq l \leq 100$, $32 \leq l_1 \leq 74$ and $20 \leq l_2 \leq 50$, with the constraint

$l_2 \leq 0.75l_1 - 2.5$), the primary analysis was carried out coming to a total of 50,000 tested design combinations.

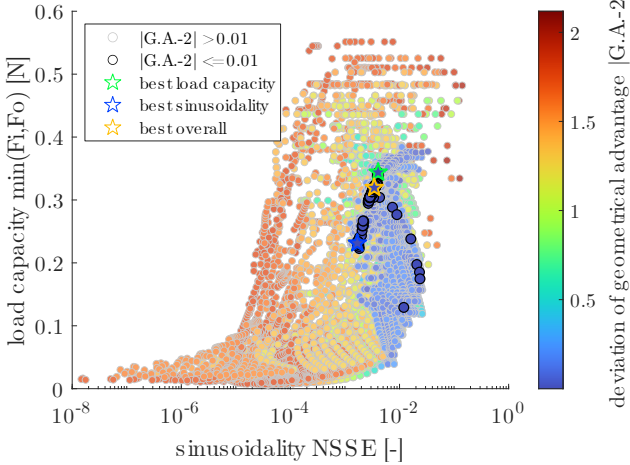


Fig. 5: Best performing designs. Sinusoidal normalized sum of square error, Sinusoidal NSSE, versus load capacity, minimum of input force with output constrained and output force with input constrained for 1% of the input displacement, $\min(F_i, F_o)$, versus the deviation of the geometrical advantage, $|(\text{G.A.}) - 2|$.

For now, we have explored the complete design space with a preliminary investigation that allowed us to more efficiently explore promising areas with the primary investigation. As this still left room for improvement regarding the resolution between the parameters in the simulations and the criteria, multiple iteration steps were performed with two goals in mind. Firstly to narrow down the search space, allowing for higher resolution searches in narrower spaces. While concurrently tightening the constraints, in order to converge to improved designs (for details see Supplementary material).

The results presented in Fig. 5 demonstrate that achieving the set constraint on the geometrical advantage requires making compromises between sinusoidality and the load capacity. Furthermore, it can be observed that high sinusoidality is only achievable with a low load capacity and G.A.. Conversely, designs with optimal load capacity do not perform well in terms of the other criteria. For the set constraint on the G.A. the resulting designs (highlighted with black contours), can only be found in a small area of the full criteria space. Three designs are indicated, first of all, the design with the best load capacity $(\alpha, l, l_1, l_2) = (29.5^\circ, 38.4, 71.8, 41.8)$ for which $G.A. = 2.010$, load capacity $F_c = 0.344\text{ N}$ and sinusoidality $SSE = 1.7 \times 10^{-3}$. Secondly the design with the best sinusoidality $(\alpha, l, l_1, l_2) = (16.2^\circ, 26.3, 67.8, 23.6)$ for which $G.A. = 1.992$, load capacity $F_c = 0.2313\text{ N}$ and sinusoidality $SSE = 4.1 \times 10^{-3}$. And lastly, the design that takes the compromise in both to get a better overall behavior $(\alpha, l, l_1, l_2) = (24.8^\circ, 32.7, 71.2, 34.8)$ for which $G.A. = 1.9993$, load capacity $F_c = 0.3195\text{ N}$ and sinusoidality $SSE = 3.4 \times 10^{-3}$.

Looking at the parameters of these designs again indicates that an increase in the angle of the flexures (α) generally increases the load capacity while worsening the sinusoidality (see also Fig. S18). And furthermore,

an increase in the flexure length (l) has a bad influence on the load capacity while improving the sinusoidality (see also Fig. S16-S17).

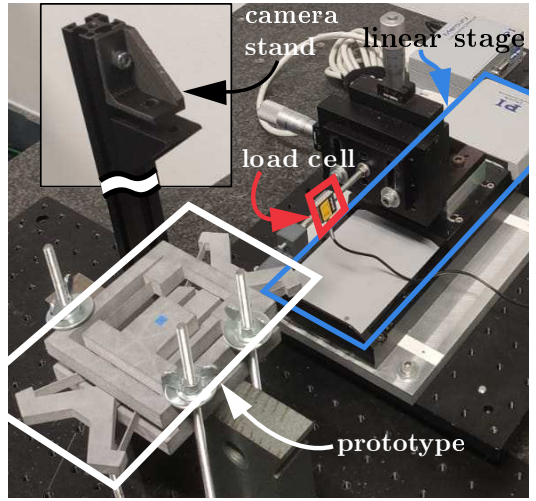


Fig. 6: Experimental setup with prototype. The experimental setup used for validation of the prototype.

Validation

To validate our findings, a prototype, $(\alpha, l, l_1, l_2) = (26.1^\circ, 40.2, 72.6, 37.7)$, of the mechanism was fabricated using Multi Jet Fusion (MJF) and the material Polyamide 12. The prototype was then subjected to tests on the displacement relation and force-displacement by giving an input displacement with a linear stage and measuring the resulting input force with a load cell and the output displacement by tracking a marker (see Fig. 6), of which the results are presented in 7. In order to provide a better representation of the prototype's behavior, the tests were performed over a larger domain than was used in the FE simulations. Subsequently, the simulation was updated to incorporate this modified domain, while simultaneously the flexure thicknesses were modified to more realistically represent the measured thickness inaccuracies of the flexures associated with the manufacturing process. Additionally, as the prototype showed viscoelastic characteristics, such as hysteresis, creep, and stress relaxation the results were averaged over multiple tests (see Supplementary material for more details).

As is evident in Fig. 7B while comparing the simulation and experimental validation design, especially the behavior of the prototype before the transition area, the area where the stiffness vastly changes, shows a very different force-displacement correlation to the simulation. This is attributed to the fact that in the simulations due to the rigid assumption of the bulk structure, any applied input force is transmitted fully onto the butterfly flexures such that the critical buckling load occurs sooner. And while for the experimental results, it is evident that the stiffness of the structural parts of the prototype can not be assumed as infinite, the critical load, as seen as input force, needed for buckling is still comparable (see also Fig. S12). Additionally, the behavior around and after the transition area, where the behavior of the mechanism is not dictated

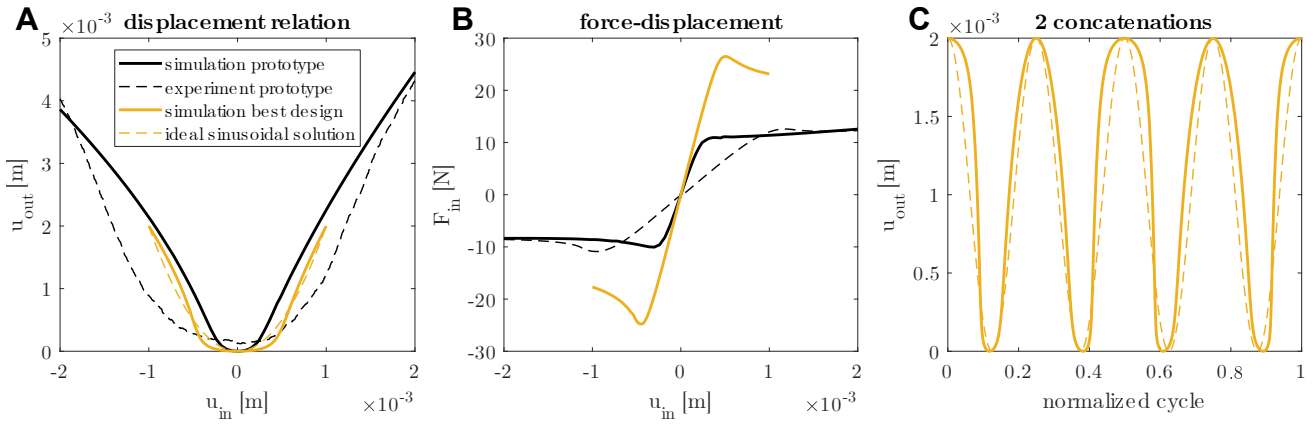


Fig. 7: Validation and the best design (A) Input-output displacement relation for the simulation and experimental result of the prototype (α, l, l_1, l_2) = (26.1°, 40.2, 72.6, 37.7), the best overall design (α, l, l_1, l_2) = (24.8°, 32.7, 71.2, 34.8) and the ideal sinusoidal solution. (B) Force-displacement graph. (C) Theoretical output displacement versus time for two concatenated frequency doublers, for the ideal sinusoidal input.

by the stiffness of the structure but rather that of the flexures, is in good agreement with the simulation results. Furthermore, inaccuracies in manufacturing and measurements together with the viscoelasticity of the used material also attribute to the lack of correlation between the simulation and experimental result of the prototype (see also Fig. S11 and Fig. S13).

Examining the displacement relation for the manufactured prototype (see Fig. 7 A), it becomes evident that due to the decrease in stiffness before the transition area, the actual prototype has a delayed output displacement increase compared to the simulations (see also Fig. S12). This also leads to almost no output displacement for a relatively large area around the equilibrium point. Furthermore, it can be seen that the experimental result has a more symmetrical response than that shown in the simulations.

Furthermore, analyzing the displacement relation of the best overall design found and comparing it to the ideal sinusoidal solution it can be observed these do not match up perfectly. This is caused by the compromise on the sinusoidality, in order to achieve a better geometrical advantage and load capacity.

Lastly, observing the output displacement after two concatenations, presented in Fig. 7 C, it is evident that the amplitude of the best design is similar to the ideal amplitude, due to the small deviation of the G.A. in the best design. Additionally, the variation in frequency over the normalized cycle, due to the added non-sinusoidalities visible in the displacement relation, is clearly observable for the best design.

Further recommended research could be conducted on exploring methods to increase the relative stiffness of the structure compared to the flexures through advanced manufacturing techniques. Furthermore, a deeper investigation into the impact of viscoelasticity on the behavior of the frequency doubler can be undertaken. Finally, research on solving the problem of parity causing highly nonlinear force-displacement behavior when preloading, by statically balancing the frequency doubler building block would be of interest (see also Fig. S5).

Conclusion

In summary, an eight-bar mechanism-based frequency doubler has been explored that utilizes displacement around a singularity to double the input frequency. We have analyzed the influence of the geometry of the frequency doubler on its behavior and have shown how to establish criteria that allow for concatenation. Using these criteria geometrical parameters were identified, allowing for effective concatenation. A prototype was manufactured to validate the displacement and force-displacement relation. The resulting force-displacement indicates a good correlation between the simulation and the prototype's response after the transition area. However, due to the rigid body assumption of the structure in the simulations, the stiffness before this is substantially higher in the simulations. The result of this also shows itself in the displacement relation where due to the delayed buckling of the butterfly flexures the output displacement increase is also delayed. Resulting, in almost no displacement around the equilibrium. Additionally, a theoretical best overall design is identified, indicating the possibilities for efficient concatenation.

When concatenated these mechanisms not only solve the coupling between footprint and range of motion through frequency multiplication but due to their inherent storing of strain energy could embed both functions into a monolithic architected material, which could form the basis for new energy storage and actuation methods highly desirable in the field of soft robotics.

Material & Method

Details on the design can be found in section S1. The method for setting up the simulations is detailed in section S3. Further explanations on the fabrication and experimental setup and validation of the design and prototype are reported in section S4.

Supplementary Materials

Section S1: Design

Section S2: Criteria

Section S3: Simulations

Section S4: Fabrication & Testing

Section S5: Additional results

Section S6: Scripts

Fig. S1 Frequency doubler design.

Fig. S2 Frequency doubler deformation.

Fig. S3 Behavior of a frequency multiplier for a deviation in the geometrical advantage.

Fig. S4 Behavior of a frequency multiplier for a deviation in sinusoidality.

Fig. S5 Behavior of the frequency doubler indicating its opposing parity.

Fig. S6 Lines and keypoints of the simulation.

Fig. S7 Deformation in FEM $u_{in} = 1 \text{ mm}$.

Fig. S8 Scatter plots with all concatenation criteria showing the iteration process.

Fig. S9 Manufactured design part.

Fig. S10 Image of the experimental setup.

Fig. S11 Experimental data compared with simulation data.

Fig. S12 Experimental data compared with new non-rigid simulation.

Fig. S13 Experimental data showing viscoelasticity of the prototype.

Fig. S14 Deformation experiment $u_{in} = 1 \text{ mm}$.

Fig. S15 Deformation experiment $u_{in} = 2 \text{ mm}$.

Fig. S16 Mechanical response of the frequency doubler regarding the criteria for the preliminary investigation.

Fig. S17 Full mechanical response of the frequency doubler regarding the geometrical advantage for the preliminary investigation.

Fig. S18 Full mechanical response of the frequency doubler regarding the sinusoidality for the preliminary investigation.

Fig. S19 Full mechanical response of the frequency doubler regarding the load capacity for the preliminary investigation.

Fig. S20 Scatter plots of all data for multiple different criteria.

Fig. S21 Displacement relation, force-displacement relation, and output upon theoretical concatenation of the best designs.

Table 1 Design parameters.

Table 2 Best points for each iteration step.

Movie S1 (.mp4 format). Displacement of the prototype during the experiment.

Movie S2 (.avi format). Displacement of the FEM simulation.

Movie S3 (.avi format). Displacement of the non-rigid FEM simulation.

References

- [1] C. A. Aubin, B. Gorissen, E. Milana, P. R. Buskohl, N. Lazarus, G. A. Slipher, C. Keplinger, J. Bongard, F. Iida, J. A. Lewis, and R. F. Shepherd, "Towards enduring au-

tonomous robots via embodied energy," *Nature*, vol. 602, no. 7897, pp. 393–402, 2022.

- [2] D. Rus and M. T. Tolley, "Design, fabrication and control of soft robots," *Nature*, vol. 521, no. 7553, pp. 467–475, 2015.
- [3] P. Boyraz, G. Runge, and A. Raatz, "An overview of novel actuators for soft robotics," *High-Throughput*, vol. 7, no. 3, pp. 1–21, 2018.
- [4] S. Coyle, C. Majidi, P. LeDuc, and K. J. Hsia, "Bio-inspired soft robotics: Material selection, actuation, and design," *Extreme Mechanics Letters*, vol. 22, pp. 51–59, 2018.
- [5] S. I. Rich, R. J. Wood, and C. Majidi, "Untethered soft robotics," *Nature Electronics*, vol. 1, no. 2, pp. 102–112, 2018.
- [6] T. J. Jones, E. Jambon-Puillet, J. Marthelot, and P. T. Brun, "Bubble casting soft robotics," *Nature*, vol. 599, no. 7884, pp. 229–233, 2021.
- [7] A. Pal, V. Restrepo, D. Goswami, and R. V. Martinez, "Exploiting Mechanical Instabilities in Soft Robotics: Control, Sensing, and Actuation," *Advanced Materials*, vol. 33, no. 19, pp. 1–18, 2021.
- [8] D. Farhadi, J. Herder, G. Semon, and N. Tolou, "Swiss watch featuring dutch precision," *vol. Mikroniek*, no. 58(5), pp. 30–34, 2018.
- [9] N. D. Mankame and G. K. Ananthasuresh, "A Compliant Transmission Mechanism With Intermittent Contacts for Cycle-Doubling," *Journal of Mechanical Design*, vol. 129, no. 1, pp. 114–121, jan 2007.
- [10] D. N. Haridrabbai, "Towards Micro-mechanical Signal Processors : A Frequency Translator," Indian Institute of Science Bangalore, no. June, 2011.
- [11] R. Khajehtourian and D. M. Kochmann, "Soft Adaptive Mechanical Metamaterials," *Frontiers in Robotics and AI*, vol. 8, no. May, pp. 1–9, 2021.
- [12] L. Jin, R. Khajehtourian, J. Mueller, A. Rafsanjani, V. Tournat, K. Bertoldi, and D. M. Kochmann, "Guided transition waves in multistable mechanical metamaterials," *Proceedings of the National Academy of Sciences of the United States of America*, 2020.
- [13] D. Farhadi, J. L. Herder, and N. Tolou, "Frequency doubling in elastic mechanisms using buckling of microflexures," *Applied Physics Letters*, vol. 115, no. 14, 2019.
- [14] D. Farhadi, "Compliant transmission mechanisms," Delft University of Technology, p. 125, 2018.
- [15] D. Farhadi, J. L. Herder, G. Semon, and N. Tolou, "A Compliant Micro Frequency Quadrupler Transmission Utilizing Singularity," *Journal of Microelectromechanical Systems*, 2018.
- [16] L. Samuels, "A review on elastic storage mechanisms with a programmable cyclic output," 2022.

Parametric study of an elastic singularity-based frequency doubler for concatenation

Supplementary Material

Luuk Samuels

February 2023

This pdf includes:

Section S1: Design

Section S2: Criteria

Section S3: Simulations

Section S4: Fabrication & Testing

Section S5: Additional results

Section S6: Scripts

Fig. S1 Frequency doubler design.

Fig. S2 Frequency doubler deformation.

Fig. S3 Behavior of a frequency multiplier for a deviation in the geometrical advantage.

Fig. S4 Behavior of a frequency multiplier for a deviation in sinusoidality.

Fig. S5 Behavior of the frequency doubler indicating its opposing parity.

Fig. S6 Lines and keypoints of the simulation.

Fig. S7 Deformation in FEM $u_{in} = 1$ mm.

Fig. S8 Scatter plots with all concatenation criteria showing the iteration process.

Fig. S9 Manufactured design part.

Fig. S10 Image of the experimental setup.

Fig. S11 Experimental data compared with simulation data.

Fig. S12 Experimental data compared with new non-rigid simulation.

Fig. S13 Experimental data showing viscoelasticity of the prototype.

Fig. S14 Deformation experiment $u_{in} = 1$ mm.

Fig. S15 Deformation experiment $u_{in} = 2$ mm.

Fig. S16 Mechanical response of the frequency doubler regarding the criteria for the preliminary investigation.

Fig. S17 Full mechanical response of the frequency doubler regarding the geometrical advantage for the preliminary investigation.

Fig. S18 Full mechanical response of the frequency doubler regarding the sinusoidality for the preliminary investigation.

Fig. S19 Full mechanical response of the frequency doubler regarding the load capacity for the preliminary investigation.

Fig. S20 Scatter plots of all data for multiple different criteria.

Fig. S21 Displacement relation, force-displacement relation, and output upon theoretical concatenation of the best designs.

Table 1 Design parameters.

Table 2 Best points for each iteration step.

Legends for movies S1 to S3.

Other Supplementary Material includes:

(available at <https://github.com/Luuk-Samuels/ThesisLuuk/tree/main/Movies>)

Movie S1 (.mp4 format). Displacement of the prototype during the experiment.

Movie S2 (.avi format). Displacement of the FEM simulation.

Movie S3 (.avi format). Displacement of the non-rigid FEM simulation.

Section S1: Design

The design of the eight bar mechanism based frequency doubler using singularity is shown in Fig. S1. The mechanism consists of three parts, the input shuttle (in blue), allowing for linear horizontal motion, the butterfly mechanism (in green), which moves around a singularity, and the output shuttle (in purple), allowing for linear vertical motion. The mechanism exploits the movement around a singularity point in order to double the frequency. Due to the setup of the flexures, the mechanism starts in the stable singularity configuration, where the inverse kinematics of the mechanism are undefined. This can be noticed when trying to apply a displacement of the output shuttle in the positive u_{out} direction, upon which it is non-deterministic which direction the input will move. In practice, due to manufacturing imperfections or hysteresis after loading, where hysteresis makes the mechanism move in the latest loaded direction, the mechanisms will always choose a side. The deformation of the mechanism is shown in Fig. S2. It can be seen that regardless of the direction of the input displacement the output explicitly moves upwards. Meaning that for a full cycle of the input (starting at the deformed configuration for negative input (left): right-left), the output will have completed two cycles (starting in the deformed configuration (up): down-up-down-up).

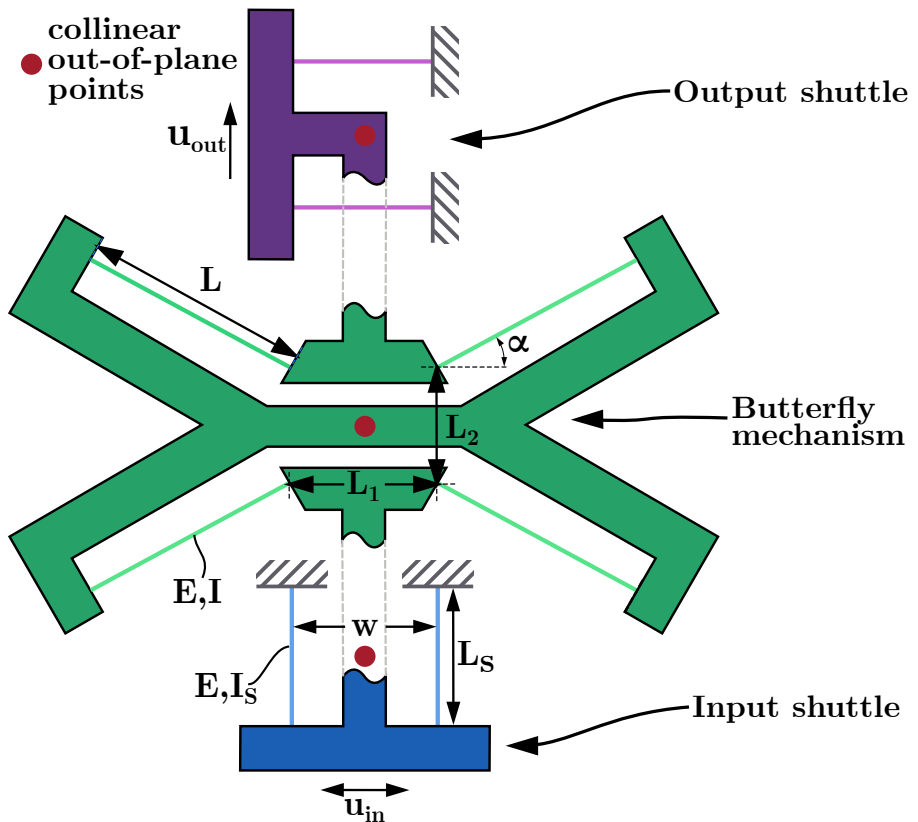


Fig. S1: Frequency doubler design. Schematic of the eight bar mechanism based frequency doubler building block with important parameters defined

The design can be fully described using the parameters shown in Fig. S1, including the thickness of all the flexures (t) and the out-of-plane (OOP) distance between the three parts (d) and the OOP breadth of the input and output plane (b_s) and the butterfly plane (b). The design variables that will be altered to tune the behavior of the mechanism are, the angle the butterfly flexures make with the horizontal axis (α), the length of the butterfly flexures (L), the horizontal distance between the butterfly flexures (L_1), and the vertical distance between the butterfly flexures (L_2). In some cases, the normalized form of these variables is taken for which they are normalized for the maximum input displacement (e.g. $l_1 = L_1/u_{in}$). The other parameters like the material properties of the mechanism, the length of the flexures of the input and output shuttle (L_s), and the width between the flexures of the output shuttle (w) are all kept constant. The design space of the variables and the constant parameters are listed in Table 1.

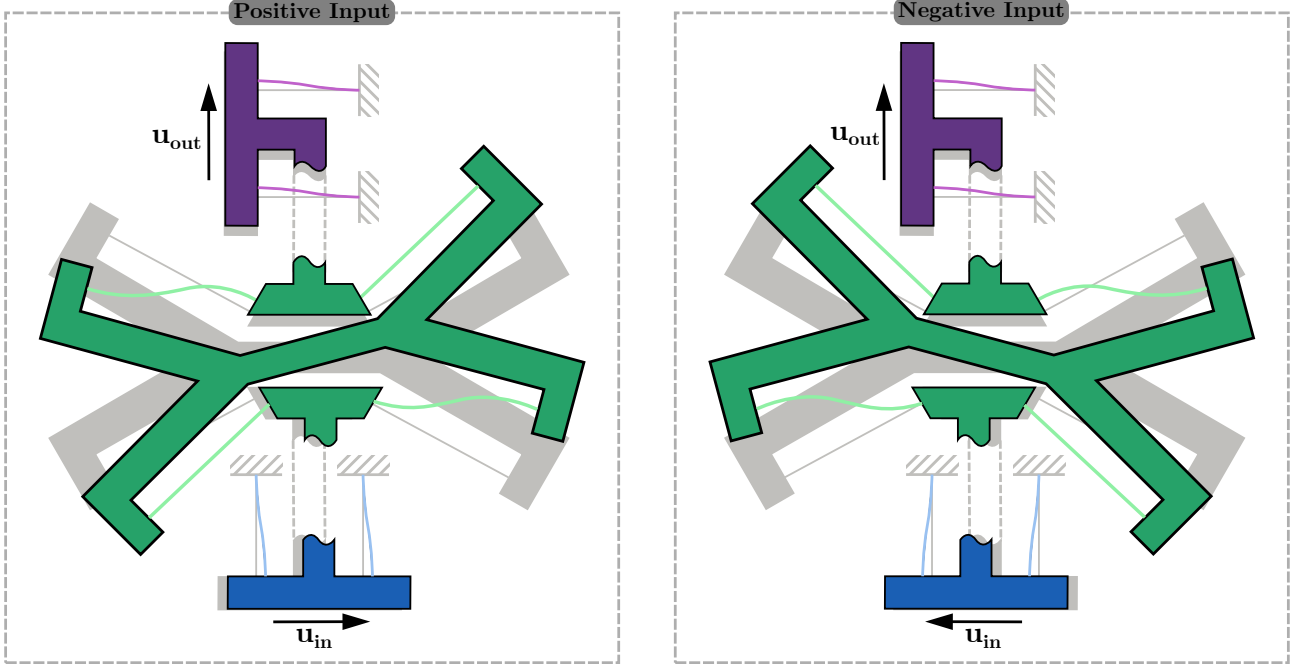


Fig. S 2: Frequency doubler deformation. Deformation of the eight bar mechanism based frequency doubler for either a positive input displacement (left) or a negative input displacement (right)

Table 1: Design parameters. Important design parameters for the eight bar mechanism based frequency doubler.

Parameters	α	L	L_1	L_2	E	I	w
Values	10-50°	10-100 mm	15-70 mm	20-70 mm	1700 MPa	$4.86 \times 10^{-13} \text{ m}^4$	60 mm
L_s	I_s	u_{in}	t	d	b	b_s	
40 mm	$7.29 \times 10^{-13} \text{ m}^4$	$\pm 1 \text{ mm}$	0.9 mm	2 mm	8 mm	12 mm	

The design space for the variables was determined systematically by having the following requirements in mind: manufacturability, compliance, functionality, and the overall footprint. The minimal length for L_1 and L_2 were for instance established with manufacturability in mind, coming from the fact that a minimal gap is needed in order to prohibit contact during operation. Additionally, L_1 and L_2 should also not be too small, to not jeopardize the rotational stiffness of the butterfly flexures, and keep functionality. The value for α was limited on both ends by the functionality of the design, as close to horizontal flexures would allow for unwanted vertical movement and vertical flexures for vertical movement. Additionally, another geometry to be aware of that would jeopardize functionality is the case where $\tan^{-1}(L_2/L_1) \approx \alpha$. For this kinematic indeterminacy, all butterfly flexures share a mutual pivot point causing an unwanted rotational degree of freedom. In order to keep the mechanism compliant, a limit was put on the minimal length of the butterfly flexures (L). Lastly, all upper limits for the length variables were set with the overall size of the design in mind.

A Design choices

As shown in Fig. S1, the center points of each of the three parts are collinear about an orthogonal OOP line with respect to the main plane. This is done to make sure the resulting moment from in-output is minimized. Similarly, the OOP distance between the planes was minimized to limit the resulting moment caused by the input force around the vertical axis. However, due to the impossibility of removing this resulting moment, the minimal distance was limited by the parasitic OOP movement of the butterfly.

Furthermore, the orientation of the structure around the input and output flexures was experimented with shortly. A diagonal connection was compared to a structure representing a T-shape, the one that was ultimately chosen (see Fig. S1). However, during operation, a small parasitic rotation around the central point occurs, which the diagonal setup could only sufficiently resist in the direction where this would cause the flexures to

tension. In the other direction, also compromised by any manufacturing imperfections in the flexures, it would cause buckling and thus loss of function. The T-shaped design always tensions and compresses one of the flexures finding a middle solution where both directions are resisted equally.

Lastly, the input and output shuttles were designed in such a way as to ensure the input force and resulting output force are applied in the center of the flexures. In order to make sure the shuttles would function as pure linear guidances.

Section S2: Criteria

In order to select the most promising design for concatenation it is important to explore what exactly is desired to achieve this. This section discusses the considered criteria and the methodology for establishing and quantifying them. First, two of the main criteria for concatenation (*G.A.* and sinusoidality) as discussed in the paper will be elaborated upon. After this, a new third important criterion regarding concatenation will be introduced and discussed (parity). After this, the most important criteria for transmission systems will be mentioned and explored (load capacity). And lastly, two new criteria important for all mechanisms will be mentioned and explored (stress and size).

A Geometrical Advantage

The geometrical advantage (*G.A.*) is the relation between the input and output displacement at the maximum of the inputs (either way). The required *G.A.* is set up such that the output displacement is twice that of the input (*G.A.* = 2). As each design is slightly asymmetric, the *G.A.* for a positive input displacement is not always the same as for a negative input displacement. Because of this, the criteria for the *G.A.* is set up to always take the side where the maximum deviation from the requirement occurs. In Fig. S3 the behavior for the ideal *G.A.* together with slight deviations is shown. As can be observed, even a slight deviation quickly grows to a much larger or smaller output displacement, due to the quadratic increase or decrease in amplitude upon concatenation. This can be problematic because it leads to input and output displacements that the design is not made for and might not be able to handle. While a *G.A.* smaller than 2 would only cause the output signal to not be perfectly sinusoidal anymore, a *G.A.* larger than 2 would lead to increased strain and if not considered while designing, could cause the mechanism to break. Additionally, due to the difference in parity of the input and output (see Section S2: C) each new concatenation would have to be preloaded differently to account for the quadratically changing operation range.

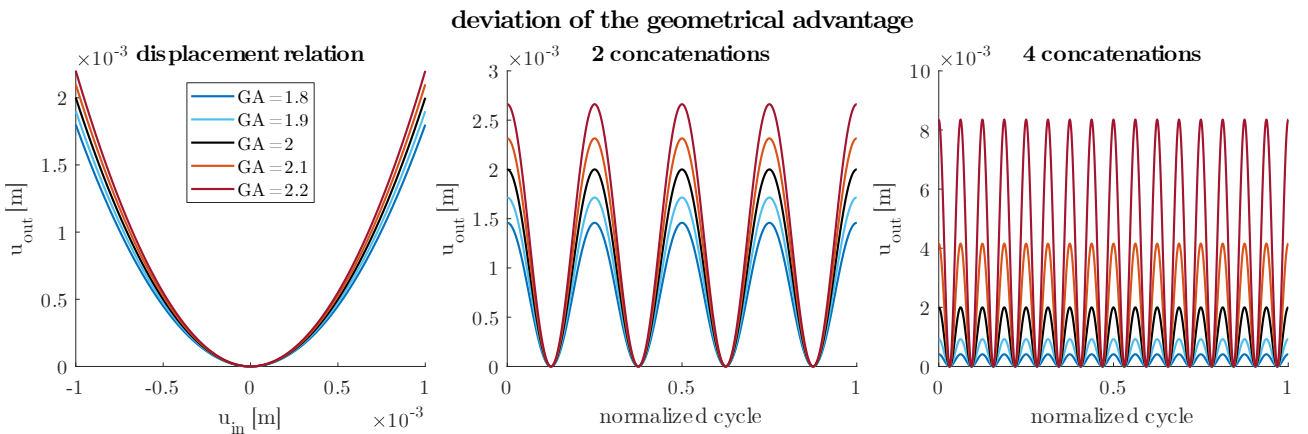


Fig. S 3: Behavior of a frequency multiplier for a deviation in the geometrical advantage. Displacement relation for different deviations from the required *G.A.* (left). The output displacement after two concatenations, for designs with a deviation in the *G.A.*, given a full cycle of an ideal sinusoidal input displacement (middle). The output displacement after four concatenations, for designs with a deviation in the *G.A.*, given a full cycle of an ideal sinusoidal input displacement (right).

B Sinusoidality

The criterion for sinusoidality quantitatively identifies the deviation from an ideal situation where a sinusoidal input would be transmitted into a sinusoidal output with twice the frequency. Even though in the literature

only linearity is mentioned as a criterion, there are multiple reasons why here it was not opted for. Firstly, a perfectly linear response from input to output is impossible due to the infinite acceleration required where the input displacement switches directions. To solve this an approximation to the ideal linear transmission can be found, however, due to the exponential growth of the non-linearity for an increasing number of concatenations this non-linearity added would quickly worsen and jeopardize the output signal of the mechanism. Secondly, a linear input signal (triangular wave) would consist of a lot of high-order frequencies in order to approximate the infinite acceleration, which could lead to unwanted resonance either in the frequency multipliers or in the application it is used in, and completely compromise the functionality. Lastly, similar to the first criterion, even if a perfect linear mechanism is acquired, a perfect linear input will also always just be an approximation.

The criterion for sinusoidality is quantified by calculating the normalized sum of square error (NSSE), between the found and the desired displacement relation. The sinusoidal normalized sum of square error:

$$SNSSE = \frac{1}{N} \sum_{i=1}^N \frac{(u_{out}(i) - f(u_{in}(i)))^2}{\max(u_{out})^2} \quad (1)$$

with

$$f = G.A. * 2000 * (\cosh u_{in} - 1) \quad (2)$$

where N is the number of substeps, and $f()$ is the ideal sinusoidal transmission function which is based on a hyperbolic cosine. This function is scaled with the $G.A.$ to keep the geometrical advantage and sinusoidality as independent criteria. The sum of square error is normalized in two ways. Firstly, to make the error independent of the number of substeps the sum is divided by the total number of substeps. In this way, the output gives an indication of the average error per substep. And secondly, to eradicate the dependency on the $G.A.$, and as such the size of the output, each error is divided by the maximum output displacement squared.

Fig. S4 shows what happens when a non-sinusoidality occurs within the signal. This is done by multiplying the perfect sinusoidal function with a linear equation, set up in the following way:

$$f_{imp}(b) = \begin{cases} (1000u_{in} + 1)b + 1 & \text{if } u_{in} \leq 0 \\ (-1000u_{in} + 1)b + 1 & \text{if } u_{in} > 0 \end{cases} \quad (3)$$

where the absolute value of b , defines the size of the non-sinusoidality added. As is evident from Fig. S4, the imperfection added makes the frequency of the signal dependent on the fraction of the cycle that is looked at. While for the full operation, the correct number of cycles can still be found (i.e. 4 after 2 concatenations and 16 after 4 concatenations). Also, notice how the increased non-sinusoidality causes the error between the ideal signal and the imperfect signal to increase, while for each quarter of the cycle, all the signals line up again. As the frequency multiplication capabilities are not directly compromised by the added imperfections this criterion will only be inspected after determining the criteria for the $G.A.$.

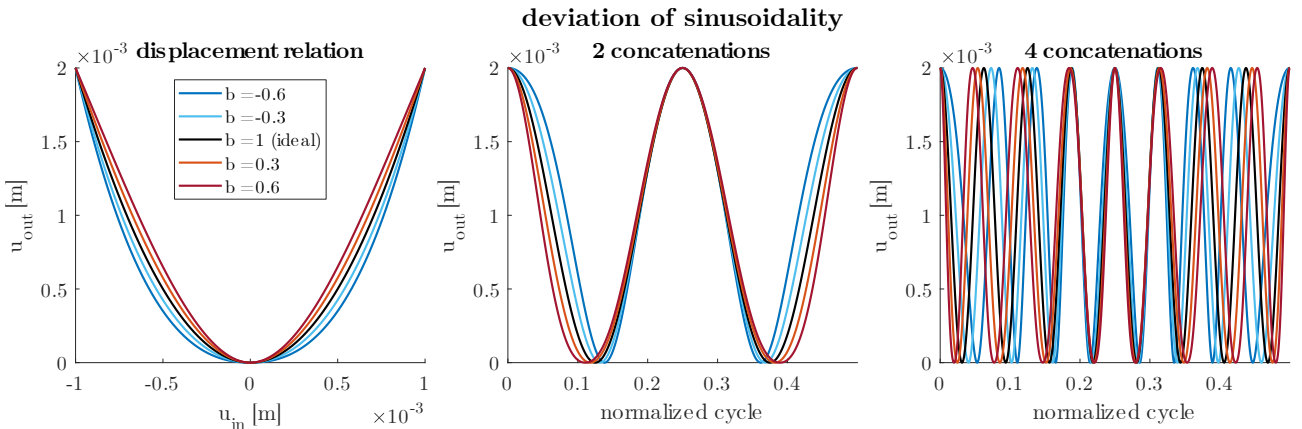


Fig. S4: Behavior of a frequency multiplier for a deviation in sinusoidality. Displacement relation for different deviations from the required sinusoidality (**left**). The output displacement after two concatenations, for designs with a deviation in the sinusoidality, given a full cycle of an ideal sinusoidal input displacement (**middle**). The output displacement after four concatenations, for designs with a deviation in the sinusoidality, given the full cycle of an ideal sinusoidal input displacement (**right**).

C Parity

The criteria for parity of a design has not been talked about in the paper, because it is a property of the frequency doubler design and can not be tuned by changing variables. Rather this criteria could be important when comparing different frequency doubler designs. It is discussed here to indicate the behavior of the explored frequency doubler, and give possible solutions.

The parity of a signal defines whether the signal is odd (i.e. $f(-x) = -f(x)$) like a sinusoidal function or even (i.e. $f(-x) = f(x)$) like a cosinusoidal function. The frequency doubler that is presented in this paper, inhibits a difference in parity between the input and output displacements. This can be observed when looking at the input and output signals (see Fig. S5). Another way to think of this is that while the input starts at the midline of the wave function the output starts at one of the maxima. For concatenation, this would mean that to allow the output to also be used as input the mechanism would have to be preloaded to make the maxima line up (see Fig. S5). This would not influence the kinematics of the designs, however, the force-displacement would have certain areas where the forces will counteract, decreasing the input stiffness, and other areas where the forces would add, leading to an increase in stiffness. This increase in stiffness requires a higher input force which could lead to stresses surpassing the yield strength of the material, making the system inoperable. A solution to solve this problem is to statically balance the frequency doubler building block such that the whole design is "zero-stiffness" and no input force is required for transmitting displacement.

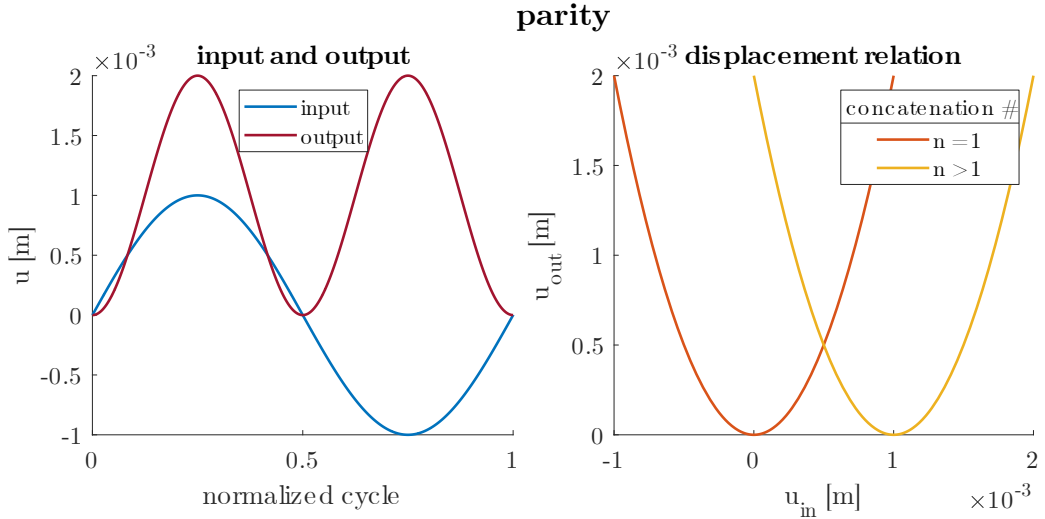


Fig. S5: Behavior of the frequency doubler indicating its opposing parity. Input displacement and corresponding output displacement of the frequency doubler, showing the transformation changing the parity (left). The required frequency doubler displacement relation for an ideal sinusoidal transmission for either an even or an odd input (right).

D Load Capacity

The criteria for load capacity determines the load the elastic frequency doubler can handle before the kinematics of the design deviates by a certain percentage (here 1%). This criterion is especially important for elastic transmission mechanisms as a high enough load on the output can completely alter the kinematics of the design. The load capacity is found by fully constraining either the input or output, to mimic an infinite load, after which a small displacement is prescribed on the output or input, and the force is read out for 1% of the original input displacement. This implies that for a kinematic deviation to not surpass 1% the load should not be higher than the measured force. Not only the load capacity of the output but also the input load capacity is evaluated because upon concatenation this load would also effectively be felt by the input shuttle. The force (input or output) for which the load capacity is minimal is used to easily quantify and compare each design. Notice that the method used here to find the load capacity is a simplification to limit the computational time. To fully test the load capacity the input or output would have to be fully constrained over the complete range of motion, however, this would be very cost inefficient while the used method gives a good representation of the capabilities. A more thorough look into how the simulations for the load capacity are set up can be found in Section S3: D.

E Stress

To make sure the mechanism would not plastically deform or even break during operation the stress read out from the simulations was compared to the yield strength of the used material. For the yield strength of PA12, the given value in the datasheet was used, $\sigma_{yield} = 48 \text{ MPa}$. A common safety factor of 1.5 was introduced to make sure the stresses would never come close to yield strength, leading to $\sigma_{max} = 32 \text{ MPa}$. To limit the computational cost the stress was only checked and read out for the maximum deformation positions in both directions, as in these positions stresses would intuitively be highest. From these two values, the maximum value was taken and compared to the maximum allowable stress.

F Size

The size of the mechanisms was calculated as if a rectangular box was placed around the mechanism from which the diagonal would indicate the size. This led to the following formula:

$$S = \sqrt{(L_1 + 2L \cos \alpha)^2 + (L_2 + 2L \sin \alpha)^2}. \quad (4)$$

The limits on size were already determined during setting up the design space, and as such this criteria was not used as a limiting criterion during the tuning of the variables. But rather to see the influence of size on the other determined criteria and to investigate possible sensitivities.

Section S3: Simulations

To gain a better understanding of the behavior of the design for different parameters inside the design space a parameter sweep of finite element method (FEM) simulations was performed using Ansys 2021 R2 in Enterprise mode. To limit the computational cost the mechanism was simplified to key points with connected lines in between (see Fig. S6).

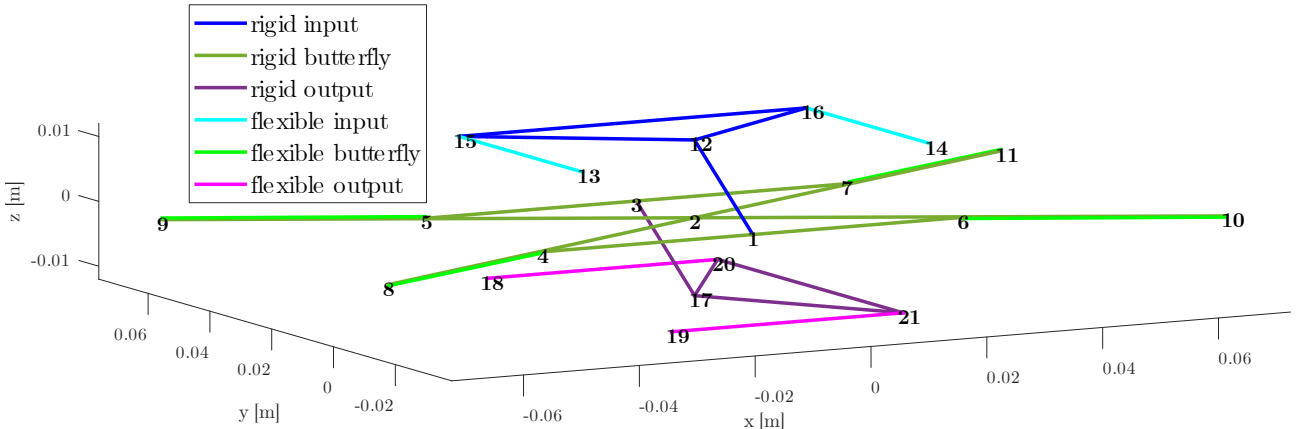


Fig. S6: Lines and keypoints of the simulation. Defined keypoints and lines, used for the simulation of the eight bar mechanism based frequency doubler

The resulting key points defined with the earlier introduced variables and parameters:

$$(x_1, y_1, z_1) = (0, 0, 0) \quad (5a)$$

$$(x_2, y_2, z_2) = \left(0, \frac{L_2}{2}, 0\right) \quad (5b)$$

$$(x_3, y_3, z_3) = (0, L_2, 0) \quad (5c)$$

$$(x_4, y_4, z_4) = \left(-\frac{L_1}{2}, 0, 0\right) \quad (5d)$$

$$(x_5, y_5, z_5) = \left(-\frac{L_1}{2}, L_2, 0\right) \quad (5e)$$

$$(x_6, y_6, z_6) = \left(\frac{L_1}{2}, 0, 0\right) \quad (5f)$$

$$(x_7, y_7, z_7) = \left(\frac{L_1}{2}, L_2, 0 \right) \quad (5g)$$

$$(x_8, y_8, z_8) = \left(-\frac{L_1}{2} - L \cos \alpha, -L \sin \alpha, 0 \right) \quad (5h)$$

$$(x_9, y_9, z_9) = \left(-\frac{L_1}{2} - L \cos \alpha, L_2 + L \sin \alpha, 0 \right) \quad (5i)$$

$$(x_{10}, y_{10}, z_{10}) = \left(\frac{L_1}{2} + L \cos \alpha, -L \sin \alpha, 0 \right) \quad (5j)$$

$$(x_{11}, y_{11}, z_{11}) = \left(\frac{L_1}{2} + L \cos \alpha, L_2 + L \sin \alpha, 0 \right) \quad (5k)$$

$$(x_{12}, y_{12}, z_{12}) = \left(0, \frac{L_2}{2}, d + \frac{b + b_s}{2} \right) \quad (5l)$$

$$(x_{13}, y_{13}, z_{13}) = \left(\frac{-w}{2}, \frac{-L_s + L_2}{2}, d + \frac{b + b_s}{2} \right) \quad (5m)$$

$$(x_{14}, y_{14}, z_{14}) = \left(\frac{w}{2}, \frac{-L_s + L_2}{2}, d + \frac{b + b_s}{2} \right) \quad (5n)$$

$$(x_{15}, y_{15}, z_{15}) = \left(\frac{-w}{2}, \frac{L_s + L_2}{2}, d + \frac{b + b_s}{2} \right) \quad (5o)$$

$$(x_{16}, y_{16}, z_{16}) = \left(\frac{w}{2}, \frac{L_s + L_2}{2}, d + \frac{b + b_s}{2} \right) \quad (5p)$$

$$(x_{17}, y_{17}, z_{17}) = \left(0, \frac{L_2}{2}, -d - \left(\frac{b + b_s}{2} \right) \right) \quad (5q)$$

$$(x_{18}, y_{18}, z_{18}) = \left(\frac{-L_s}{2}, \frac{w + L_2}{2}, -d - \left(\frac{b + b_s}{2} \right) \right) \quad (5r)$$

$$(x_{19}, y_{19}, z_{19}) = \left(\frac{-L_s}{2}, \frac{-w + L_2}{2}, -d - \left(\frac{b + b_s}{2} \right) \right) \quad (5s)$$

$$(x_{20}, y_{20}, z_{20}) = \left(\frac{L_s}{2}, \frac{w + L_2}{2}, -d - \left(\frac{b + b_s}{2} \right) \right) \quad (5t)$$

$$(x_{21}, y_{21}, z_{21}) = \left(\frac{L_s}{2}, \frac{-w + L_2}{2}, -d - \left(\frac{b + b_s}{2} \right) \right) \quad (5u)$$

In order to minimize the run time of each simulation the model is simplified by turning all the rigid lines (see Fig. S6 into fully rigid bodies using the rigid link/beam setting of the MPC184 element type. This element type uses the direct elimination method to delete the degrees of freedom at dependent nodes, thereby reducing the problem size and thus simulation time. This simplification can be made because of the relatively insignificant compliance of the rigid parts compared to the flexures, and thus does not have a big influence on the result. For the flexible parts, the BEAM188 element is used. This element uses the Timoshenko beam theory and is well-suited for slender beams. The material model used is linear, elastic, and isotropic. With a Young's modulus of $E = 1700$ MPa and a Poisson ratio of $\nu = 0.4$. All flexures are modeled as perfect rectangular beams with the thickness (t) and OOP breadth (b or b_s).

A Solver settings

Some changes compared to the standard solver settings were done to facilitate the nonlinear and large strains. First of all, NLGEOM is turned on to allow for large displacements and strains to be permitted, which are necessary for the flexure to buckle properly. Secondly, SOLCONTROL is turned on to specify the use of optimized nonlinear solutions defaults and make use of some enhanced internal solution algorithms. Thirdly, AUTOTS is turned on to make sure automatic time stepping is used. Fourthly NEQIT, which defines the maximum number of equilibrium iterations per substep, is set to 10. And lastly, NSUBST is set to 100, to make sure even with the automatic time stepping at least 100 substeps are taken.

B Imperfections

For each flexure, an initial imperfection is added to mimic some of the imperfections present in the flexures of the mechanism due to limitations in manufacturing. This was done by adding an extra node in the middle of

each flexure and prescribing a small displacement perpendicular to the length. This addition was done after in some manufactured prototypes buckling of one of the output shuttle flexures compromised the displacement of the output. Which did not correlate with what was visible in the simulations. After the addition of these imperfections buckling of the output shuttle flexures now also occurred in the simulations.

C Simulations

To restrict the full body motion of the mechanism upon the application of a displacement, key points 13,14,18, and 19 were fully constrained in all degrees of freedom. The displacement of the input was applied and read out at keypoint 12 while the output displacement was read out from keypoint 17. The simulations consist of two load steps, first, the input key point is displaced in the positive x-direction to $u_{in} = 1 \times 10^{-3}$ m. After which the same key point is displaced the same amount but in the other way. For both load steps the displacement is applied by a ramped function over the substeps, for all of which the results are read out. The stress, however, was only retrieved for the maximum deformations to limit the computational overhead. The deformation of the simplified FEM analysis from $u_{in} = -1e-3$ to $u_{in} = 1e-3$ can be seen in Fig. S7 (see also Movie S2).

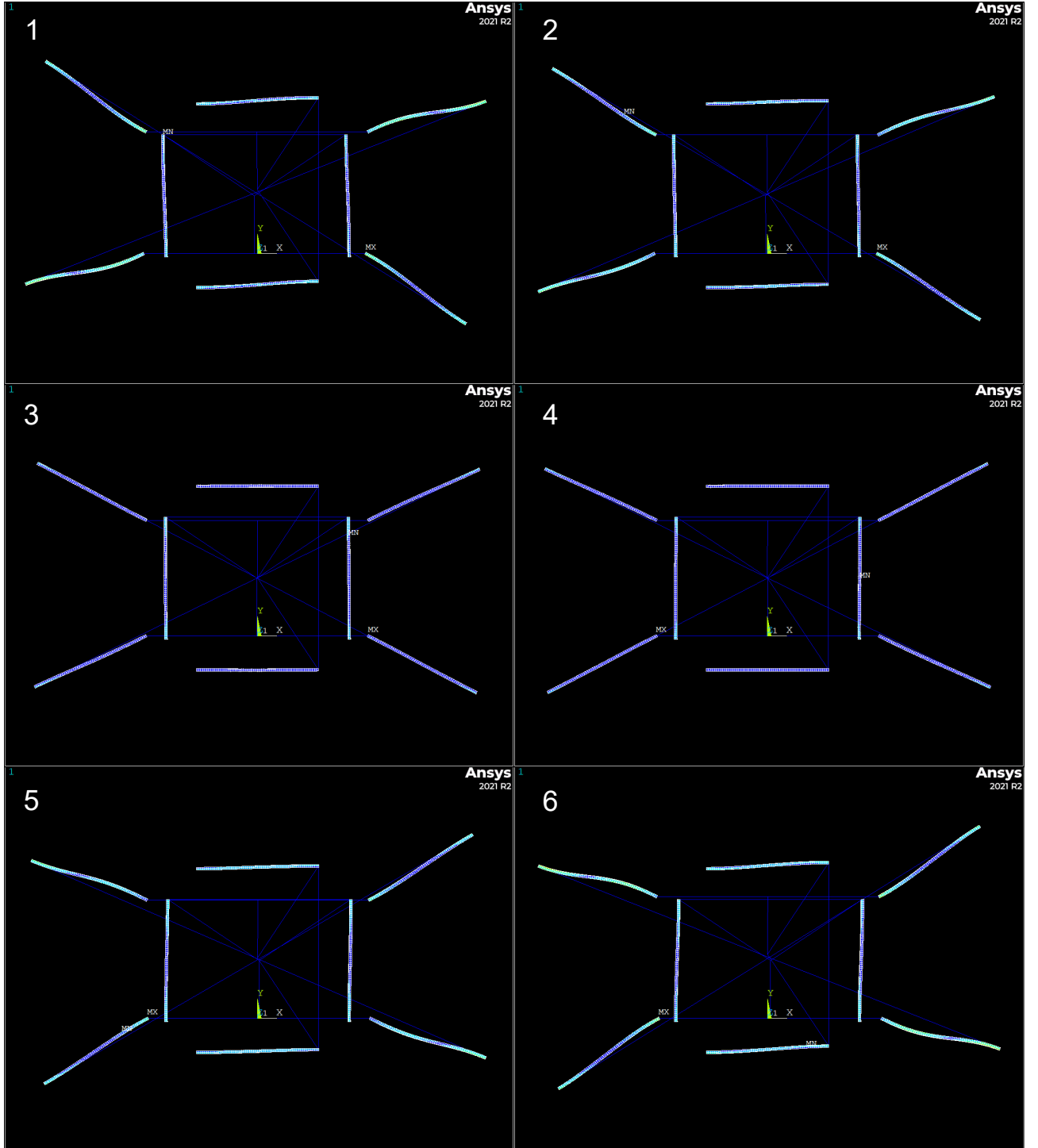


Fig. S 7: Deformation in FEM $u_{in} = 1 \text{ mm}$. Deformation of the simplified FEM model showing the complete operating range of the mechanism from $u_{in} = -1 \text{ mm}$ to $u_{in} = 1 \text{ mm}$ left to right

D Load capacity simulations

For the simulations performed for load capacity the same keypoints as for the other simulations were fully constrained (13,14,18,19). But, in addition, to find the output load capacity the output keypoint (17) was fully constrained, and likewise, for the input load capacity, the input keypoint (12) was fully constrained. After this, for the output load capacity analysis the input was displaced for 10% of the full input displacement and the force was checked for at 1% of the input displacement. For the input load capacity, the same was done, however, to not have it displace against the singularity the input key point was instead constrained to have a small (i.e. $1 \times 10^{-5} \text{ m}$) displacement in the x-direction such that it could easily move out of the singularity. In this way, a

better representational value of the input load capacity is found for the operating range of the mechanism.

E Iteration process

To improve the resolution of the design space and the performance of the criteria, multiple iterations were performed. This was done by simultaneously narrowing the design space and tightening the constraints in order to converge to the best designs. The iterations consisted of, firstly setting a hard constraint on the geometrical advantage after which the best design regarding sinusoidality, load capacity, and the best overall designs, compromising on one criterion in order to improve the other, were selected. Around these designs, a new study was started, with the resolution of each design parameter increasing by around twice that of the previous iteration. When this new study was finished, for the designs that passed the new *G.A.* hard constraint, the load capacity was also evaluated. The iteration process is visually represented in Fig. S8, while the accompanying numbers of the best designs can be found in Table 2.

As is shown, each iteration compromises the sinusoidality and load capacity behavior in order to fulfill the new geometrical advantage constraint. While each iteration also provides plentiful designs with improved criteria to be used in the next iteration for a concurrently tightened *G.A.* constraint.

The iteration process was stopped when the set limit on manufacturing accuracy was reached. This limit was set to 0.1 mm for lengths L , L_1 and L_2 , and 0.1° for angle α .

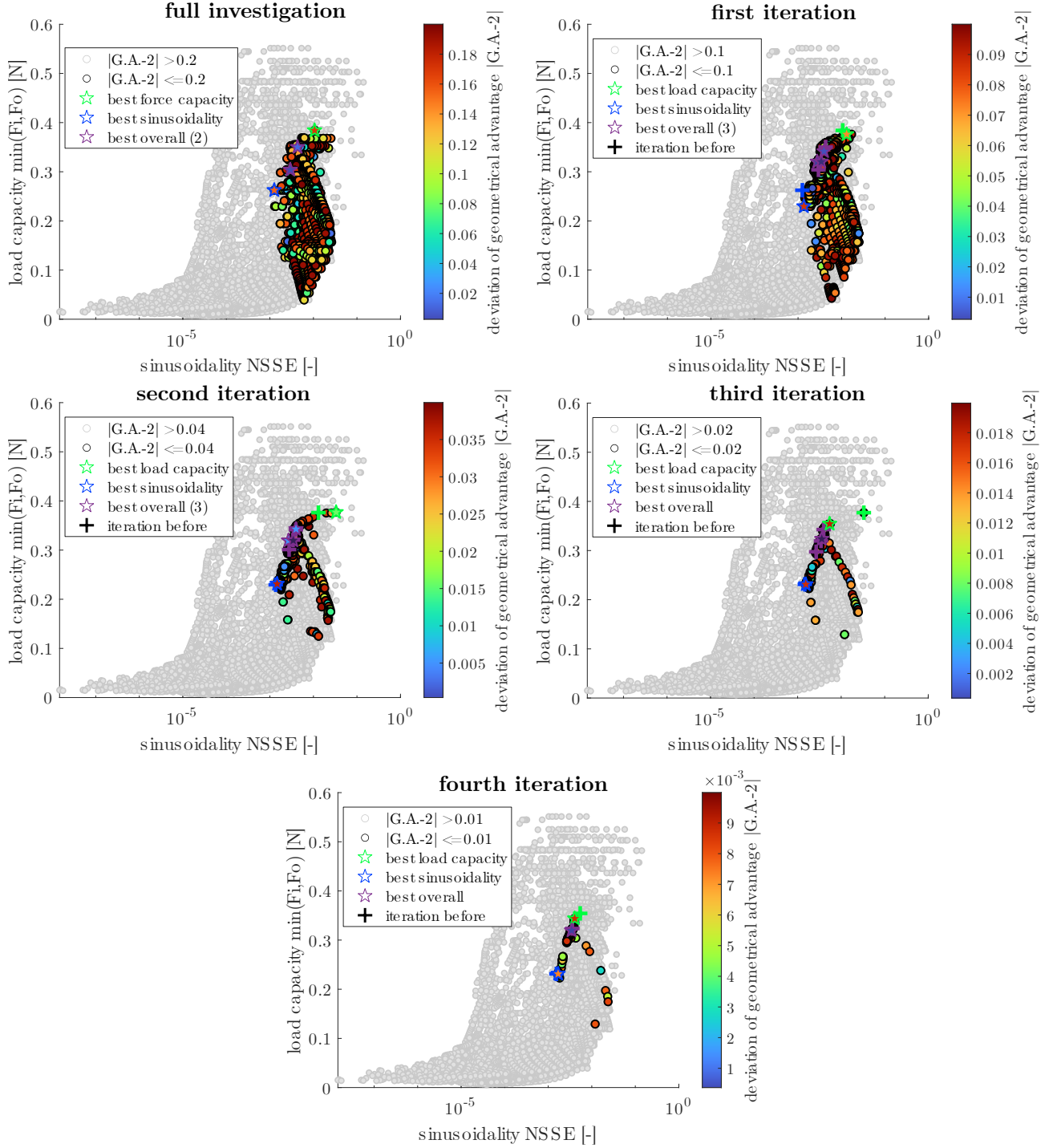


Fig. S8: Scatter plots with all concatenation criteria showing the iteration process. The sinusoidal normalized sum of square error, Sinusoidality NSSE, versus the load capacity, minimum of input force with output constrained and output force with input constrained for 1% of the input displacement, $\min(F_i, F_o)$, versus the deviation of the geometrical advantage, $|G.A. - 2|$. Shown for the start of each iteration step to define the new iteration design space. The best points selected for each iteration are listed in Table 2.

Table 2: Best points for each iteration step. List of all the best design points per iteration step, with their performance per criteria indicated.

full investigation ($1.8 < G.A. < 2.2$)							
best	G.A. [-]	load capacity [N]	sinusoidality [-]	α°	l [-]	l_1 [-]	l_2 [-]
load	1.81	0.384	1.06×10^{-2}	34	38	68	46
sin	1.83	0.262	1.26×10^{-3}	18	26	68	26
overall (1)	1.98	0.304	2.94×10^{-3}	24	34	71	34
overall (2)	1.97	0.3502	4.3×10^{-3}	30	38	71	42
first iteration ($1.9 < G.A. < 2.1$)							
best	G.A. [-]	load capacity [N]	sinusoidality [-]	α°	l [-]	l_1 [-]	l_2 [-]
load	1.92	0.376	1.3×10^{-2}	33	38	69.5	45
sin	1.91	0.230	1.36×10^{-3}	16	26	68	24
overall (1)	1.993	0.301	2.76×10^{-3}	23	32	72	33
overall (2)	1.996	0.320	3.41×10^{-3}	25	33	71	35
overall (3)	1.997	0.342	3.95×10^{-3}	29.5	39	72	42
second iteration ($1.96 < G.A. < 2.04$)							
best	G.A. [-]	load capacity [N]	sinusoidality [-]	α°	l [-]	l_1 [-]	l_2 [-]
load	1.981	0.377	3.30×10^{-2}	33.4	38.6	69.7	44.8
sin	1.960	0.231	1.46×10^{-3}	16	25.7	68.2	23.6
overall (1)	1.992	0.298	2.67×10^{-3}	22.6	31.7	72.2	32.6
overall (2)	1.999	0.320	3.44×10^{-3}	24.8	32.7	71.2	34.8
overall (3)	2.01	0.343	3.97×10^{-3}	29.5	38.7	72.4	42.4
third iteration ($1.98 < G.A. < 2.02$)							
best	G.A. [-]	load capacity [N]	sinusoidality [-]	α°	l [-]	l_1 [-]	l_2 [-]
load	2.020	0.354	5.4×10^{-3}	30	37	70.5	41.5
sin	1.981	0.231	1.5×10^{-3}	16	25.7	68.3	23.5
overall	1.9996	0.3236	3.6×10^{-3}	25.4	33.3	70.8	35.4
fourth iteration (final) ($1.99 < G.A. < 2.01$)							
best	G.A. [-]	load capacity [N]	sinusoidality [-]	α°	l [-]	l_1 [-]	l_2 [-]
load	2.010	0.344	4.1×10^{-3}	29.5	38.4	71.8	41.8
sin	1.992	0.2313	1.7×10^{-3}	16.2	26.3	67.8	23.6
overall	1.9993	0.3195	3.4×10^{-3}	24.8	32.7	71.2	34.8

Section S4: Fabrication & Testing

To validate the simulations performed, a prototype was manufactured and tested. In this section, first, the manufacturing process will be elaborated upon after which details on the testing setup and process will be given.

A Fabrication

During the fabrication of the design all the non-flexible parts, to mimic the rigidity assumed in the simulations, were made sufficiently thick. The schematic of the 3D part that was manufactured is shown in Fig. S9, while the manufactured prototype is shown in Fig. S10.

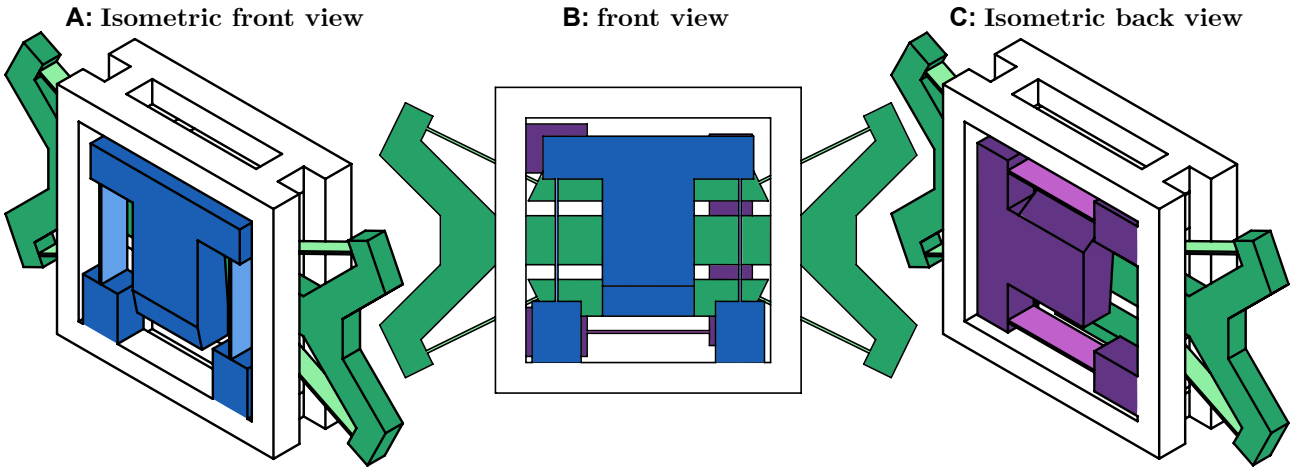


Fig. S 9: Manufactured design part. Different angles of the manufactured part, with the input shuttle (blue), the output shuttle (purple), and the butterfly mechanism (green)

The design was manufactured using Multi-Jet fusion 3D printing out of PA-12 (Young's modulus $E = 1700 \text{ MPa}$, Poisson's ratio $\nu = 0.4$ and Yield strength $\sigma_{yield} = 48 \text{ MPa}$) which is flexible enough to support high strain in the flexures. This manufacturing method uses a powdered bed which means no support structure is needed, but still allows a design as complex as the one given to be printed with high resolution ($\pm 0.3 \text{ mm}$). Also needing no support structure means the risk of breaking a flexure during the removal of a support structure is averted. This manufacturing method also allows for large maximum part dimensions while still having high-density and low-porosity full-infill printing with predictable material properties.

B Testing

To validate the performed FEM simulations the manufactured prototype was tested and the results were compared with the found force and displacement data from the simulations. During the experiments, a linear input motion was applied while the input force and output displacement were measured. A picture of the experimental setup used can be found in Fig. S10.

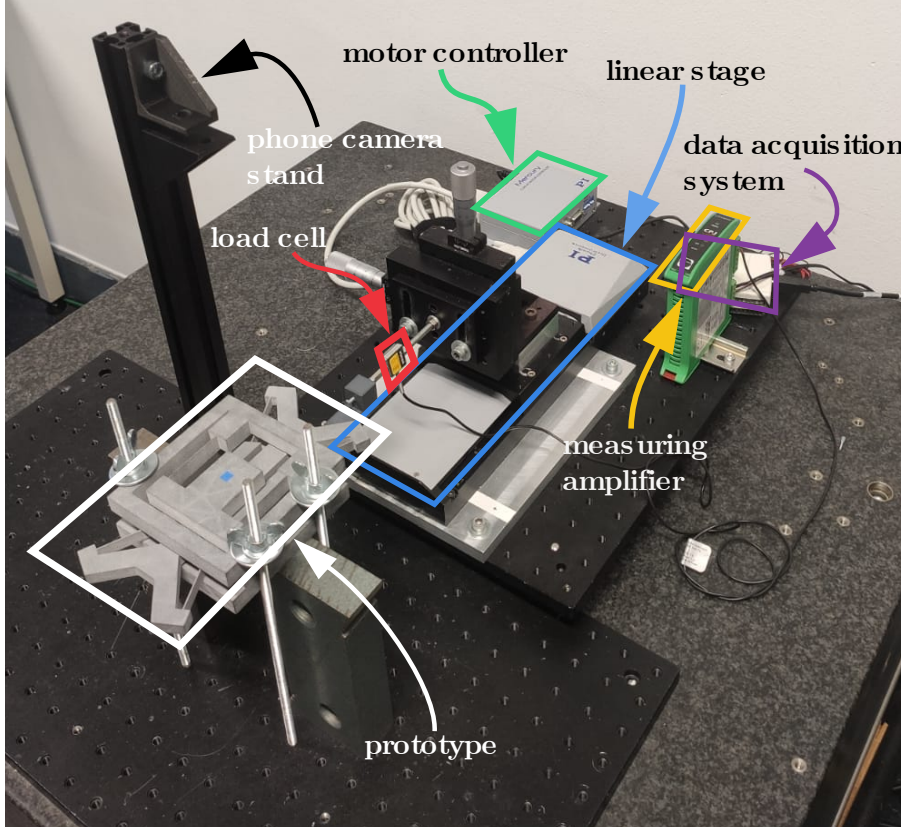


Fig. S 10: Image of the experimental setup. Experimental setup to find the input-output displacement and input force used to validate the simulations.

To apply a perfect linear input displacement PI M505.4DG low-profile translation stage was used. This translation stage has a design resolution of $0.017\text{ }\mu\text{m}$ and zero-backlash due to the recirculating ball screw drive. This motion stage was controlled using a PI mercury motion controller. To measure the force that was put at the input a FUTEK LSB200 FSH03875 was attached between the mechanism and the stage. This load cell can handle forces up to 45 N and has a maximum inaccuracy of $\pm 0.25\%$ of the rated output, due to some nonlinearity, hysteresis, and nonrepeatability. Last, the output displacement was measured using a 48MP phone camera, which filmed a blue dot attached to the mechanism which using video processing could be tracked. From this, using the number of pixels in the image and a known dimension of the design, the output displacement could be extracted.

Data processing

As can be seen in Fig. S11 (dotted lines) the mechanism suffers from viscoelastic behavior such as hysteresis, creep, and stress relaxation. This shows itself in each cycle with behavior changes depending on the previous deformation state. For all the cycles the actuation speed was constant and set to the slowest setting available for the test setup. To give a more representative behavior of the mechanism the average of the four explored cycles was taken. These cycles consist of a positive and negative cycle starting in the origin, and two cycles starting in the most deformed positions. Furthermore, the flexure thicknesses of the original simulation were updated to allow for a better comparison to the manufactured prototype. For this, the thicknesses of the manufactured flexures were measured using a digital caliper for multiple different positions on the flexures. From the measurements, it became clear that the thickness of the flexures was not constant over their length, and especially close to their connection point the thickness had quite a significant manufacturing inaccuracy. To account for this a representative effective thickness value was selected close to the minimal thickness measured. For the updated simulation, the thickness of the butterfly flexures was changed from $t = 0.9\text{ mm}$ to $t = 0.75\text{ mm}$. The resulting change is shown in Fig. S11. While this change only has a very slight effect on the displacement relation behavior, a larger influence can be seen in the force-displacement relation. This change is can be explained by the critical buckling load of the butterfly flexures lowering, due to the decreased effective stiffness. Only the flexure thickness was changed as other small changes in the other variables have relatively little influence.

Inspecting the hysteresis behavior in the displacement relation of all the cycles, it is shown that especially whenever the mechanism moves from the equilibrium position into the deformed state (either way), a large flat area where the output displacement changes only marginally can be seen. This area almost completely disappears when the mechanism moves in the opposite direction. This can be explained by the fact that the critical buckling load of the butterfly flexures, which first has to be reached before the output starts moving is delayed due to the elastic hysteresis behavior and the effective decrease in stiffness of the prototype due to the non-rigidity of the structure, while for the opposite direction, the output is already displaced and as such the critical buckling load does not have to be reached.

The result of this can also be seen when looking at the force-displacement of the prototype. When moving from the equilibrium to the deformed state a clear buckling behavior is shown, while moving in the opposite direction this behavior mostly disappears. Additionally, when moving from the equilibrium position the transition area where buckling occurs happens for a larger displacement than when moving back.

Lastly, examining the behavior of the prototype the displacement relation has a slight non-symmetry for positive or negative input. This is also shown in the force-displacement, where after the transition area for a positive input displacement the force still increases while for a negative input, the force is almost constant. This non-symmetry is caused by the output shuttle in both the simulation and prototype not being symmetrical over the vertical axis. When inspecting the behavior between the experimental results and the updated simulation the effect of this non-symmetry is comparable when looking at the force-displacement. However, looking at the displacement relation, the non-symmetry of the simulation is way more pronounced and causes the geometrical advantage for a negative input to be lower than expected.

Further comparing the force-displacement between the updated simulation and the experiments, it is clear that the stiffness before the transition area is a lot higher for the simulation than the experimental results. This can be explained by the fact that in the simulation the whole mechanism is modeled as fully rigid. This means that all the force from the input is directly transferred to the butterfly flexures, causing the critical buckling load to be reached a lot earlier. In the manufactured mechanism this high stiffness assumption relative to the elastic flexures clearly does not hold resulting in lower stiffness and a longer displacement before buckling is reached. This is mostly caused by limited stiffness of the manufactured prototype, but some inaccuracy can also be attributed to manufacturing and measuring inaccuracies in combination with the viscoelasticity of the material. In contrast, the critical buckling load between the simulation and experiment does match. The influence of the non-rigidity of the prototype also shows itself in the displacement relation, where around the equilibrium the output displacement stays very small for a larger area than the simulation would indicate.

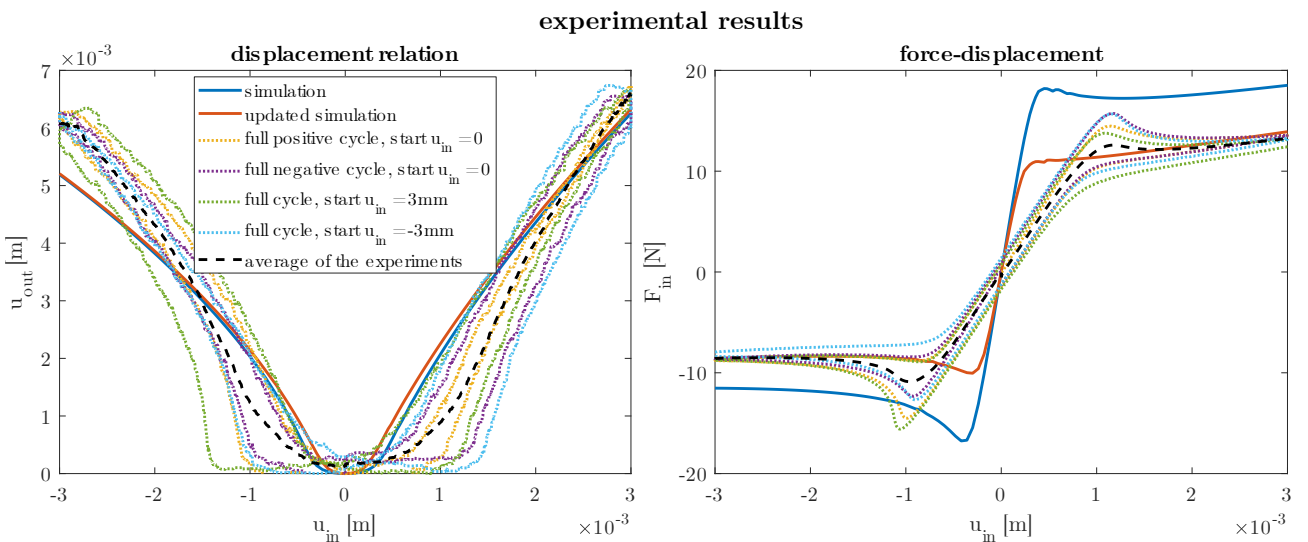


Fig. S 11: Experimental data compared with simulation data. Displacement relation and force-displacement of the original simulation, the simulation with the flexure thicknesses updated to match the prototype, and experimental data of a full cycle for four different starting positions.

Non-rigidity assumption

To further investigate the influence of non-rigidity in the prototype compared to the FEM simulations, another study was conducted of which the result is shown in Fig. S12. For this analysis, the full 3D part (see also Fig.

S9) with similarly updated flexure thicknesses as the updated simulation was imported into Ansys, the bottom of the structure was fully constrained to mimic the connection during testing and the input was displaced by 3 mm either way. Furthermore, the solver settings used were kept the same as the original simulations (see also Movie S3).

As is evident from the force-displacement relation the stiffness of the device for the non-rigid simulation has indeed as expected decreased, while the stiffness after the transition area is close to identical. Also when examining the displacement relation the expected flattening around the equilibrium point is clearly visible, due to the buckling occurring later. This further validates that the non-rigidity in the prototype causes the simulation to not fully correlate. This also shows the sensitivity of the design to non-rigidity and, taking manufacturing inaccuracies in mind could further explain the still present difference for both the force-displacement and displacement relation.

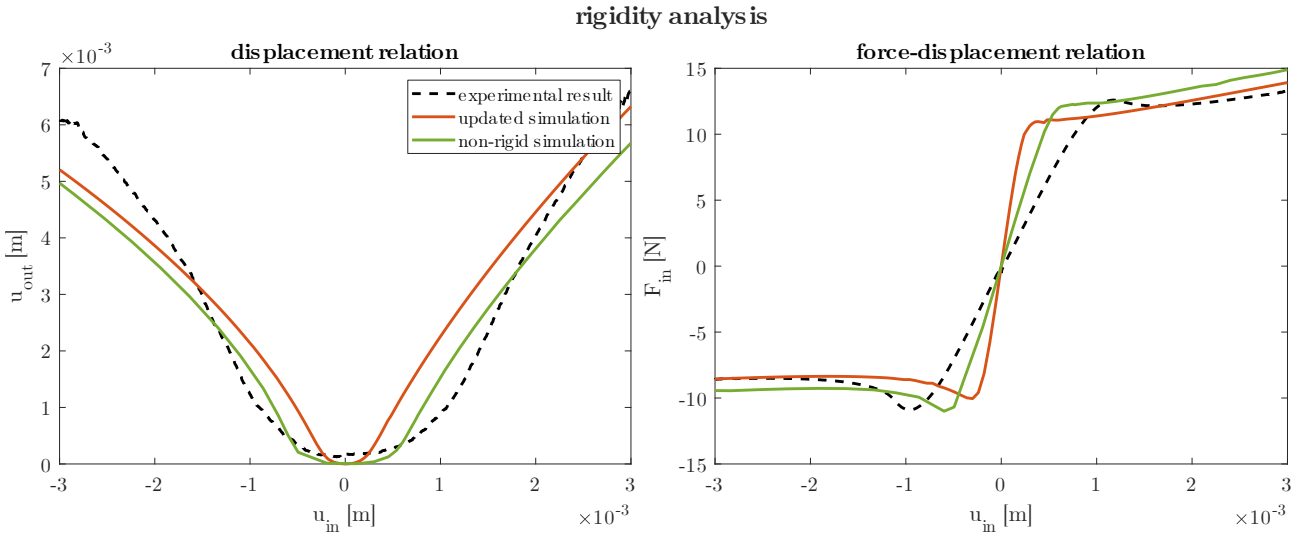


Fig. S 12: Experimental data compared with new non-rigid simulation. Displacement relation and force-displacement of the averaged experimental data, the simulation with the flexure thicknesses updated, and a new non-rigid simulation of the full design.

Viscoelasticity

While some of the effects of viscoelasticity can be discerned from Fig. S11 (i.e. hysteresis and creep), due to the non-stop actuation the stress relaxation is not accounted for. To solve this a single experiment in which the mechanism was deformed to 1 mm was conducted. After the deformation was reached, the input displacement was left at this state for 5 minutes, in order to measure the stress relaxation with the load cell. Similarly, when the mechanism was displaced back into its original state, for another 5 minutes the force was still measured.

The result of this study is shown in Fig. S13. The stress relaxation behavior is clearly present, as the force decreases over time for a set displacement. The total amount of force decrease is -1.94 N , and the mechanism returned to a force of -1.66 N which was reduced to -0.21 N after the 5-minute wait. The viscoelastic effect of hysteresis is also demonstrated as the mechanism did not fully return to the original start force.

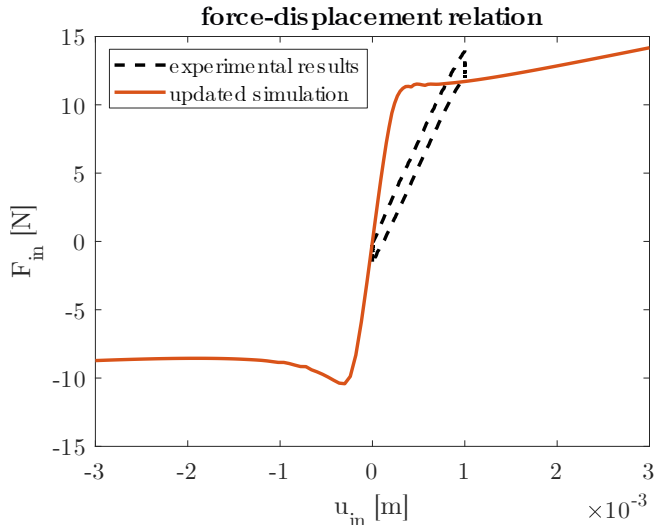


Fig. S 13: Experimental data showing viscoelasticity of the prototype. Force-displacement of the experimental data showing viscoelasticity, plotted with the simulation with the flexure thicknesses updated to match the prototype.

Deformation

The deformation over the full operating range for the prototype is shown in Fig. S 14, while in Fig. S 15 operating range is doubled to better show the buckling behavior of the butterfly flexures (see also Movie S1). As is evident upon an input displacement of $u_{in} = 1$ mm, positive or negative, the critical buckling load for the butterfly flexures has not yet been reached. However looking at the point when $u_{in} = 2$ mm, clear buckling can be seen in both directions, similar to what the experimental data (see Fig. S11) suggests.

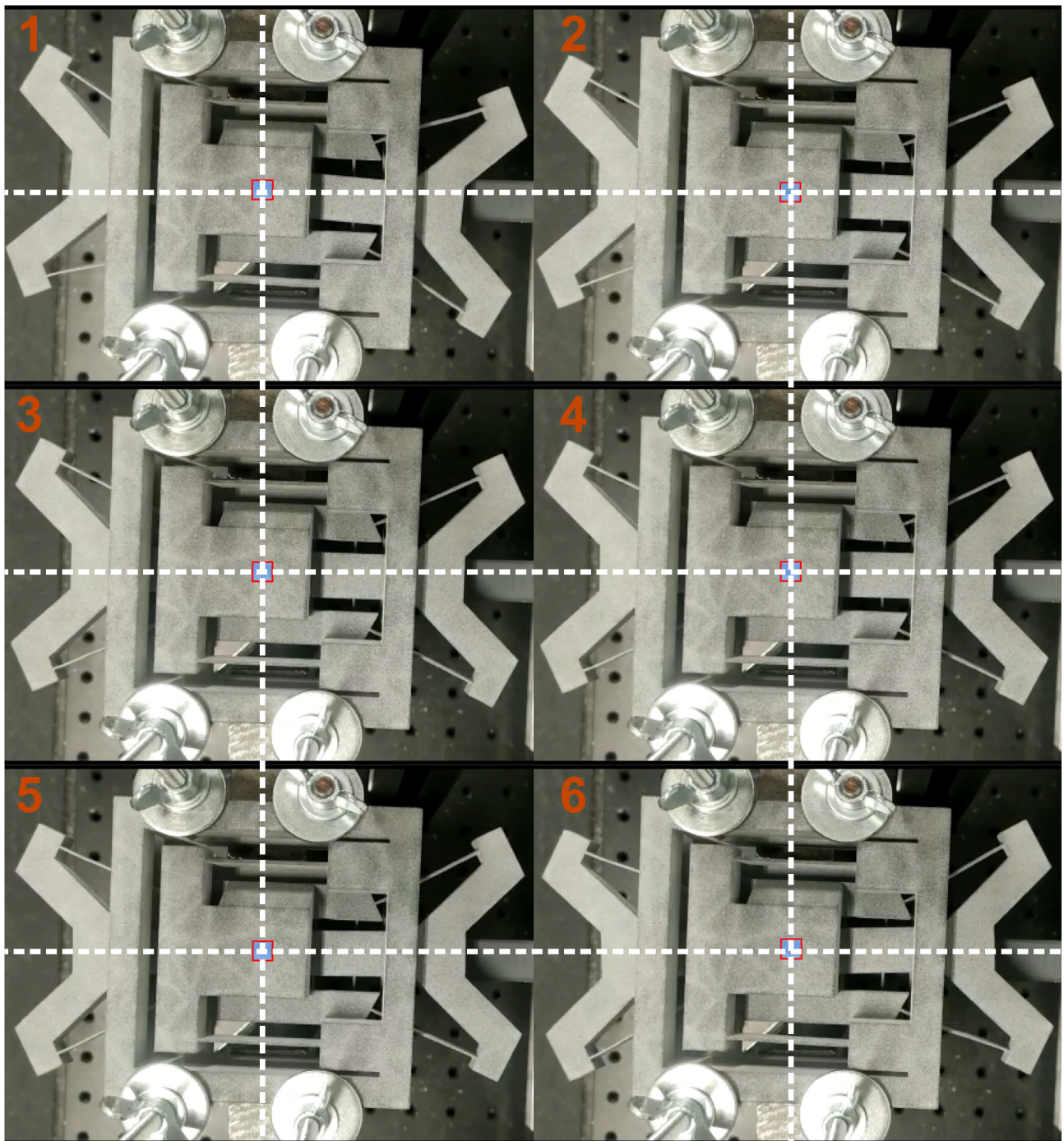


Fig. S14: Deformation experiment $u_{in} = 1 \text{ mm}$. Deformation of the prototype for the full operating range used in FEM.

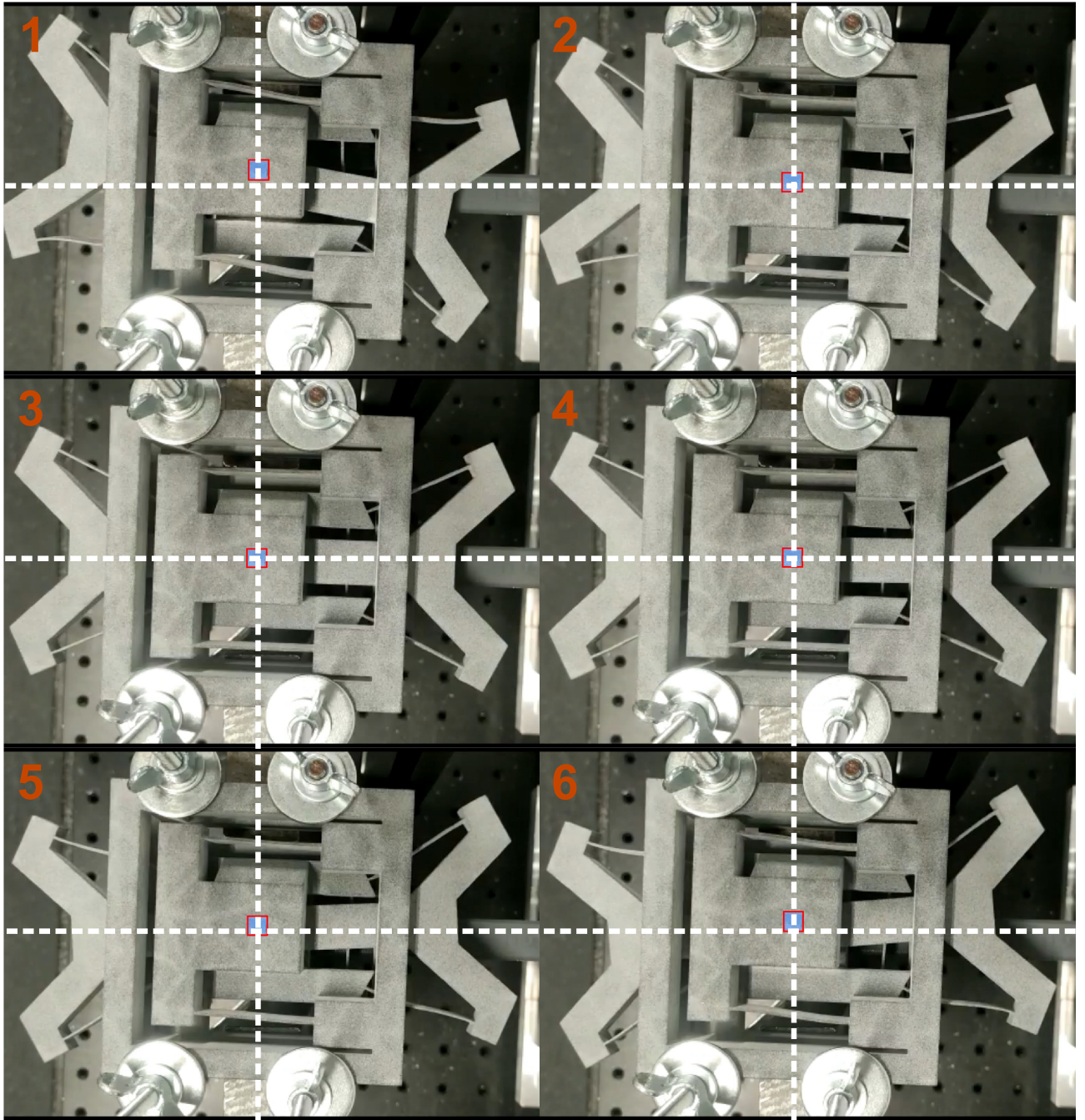


Fig. S15: Deformation experiment $u_{in} = 2 \text{ mm}$. Deformation of the prototype for twice the full operating range used in FEM.

Section S5: Additional Results

A Mechanical response of the frequency doubler for preliminary investigation

The plots for all three criteria can be seen in Fig. S16, these plots were made by selecting the best design for each of the variables of the preliminary investigation and changing the color of the square accordingly. Furthermore, the criterion for sinusoidality was not calculated in case $GA < 0.2$, which leads to the grey area that is seen in the sinusoidality plots. Additionally, load capacity designs with $l < 20$ were not taken into account, due to the high influence of the small flexure length on the load capacity, while in reality, these designs would never reach the G.A. needed to even be in contention and as such can be left out.

Looking at Fig. 16 A, there are clear areas that show promising behavior regarding the G.A., $\alpha < 40$, $l > 15$, $l_1 > 30$ and $l_2 < 50$. Furthermore, a clear correlation between l_1 and l_2 can be seen where for good geometrical

advantage behavior $l_1 > l_2$. This is caused by the fact that the arm of the output needs to be relatively higher to double the output displacement compared to the input.

The sinusoidality (see Fig. 16B) and load capacity (see Fig. 16C) also show a correlation between the horizontal and vertical spacing of the butterfly flexures. However, for the load capacity having $l_1 \approx l_2$ is preferable, while for sinusoidality similar to the G.A. it is better to have $l_1 > l_2$, but less pronounced compared to the G.A.. This can be explained by the fact that for load capacity to be high, the minimal of the input and output load capacity should be optimized, which occurs whenever the vertical and horizontal spacing is almost similar.

Looking at the other plots for sinusoidality it is clear that $30 \leq l_1 \leq 40$ shows the best behavior, while in general increasing the angle of the butterfly flexures, α , and the butterfly flexure length, l , improves the sinusoidality.

For the load capacity, the criterion also improves for increased α , however higher α jeopardizes the G.A. and as such will not result in the best design. Lastly, examining the influence of the butterfly length (l), for the G.A. a large area with promising design can be discerned, so it hardly has an impact on the optimal design for the G.A.. However, an increase in the butterfly flexure length does have a positive influence on the sinusoidality and a negative influence on the load capacity. This leads to a compromise having to be made between these two criteria to determine the butterfly flexure length.

In Fig. S17-19, the results for all the design points of the preliminary investigation are shown, to show where the most promising designs are, as well as to show where the behavior seen in Fig. S16 comes from.

Looking at the plot for the geometrical advantage, apart from the results already discussed based on Fig. S 16, a new relation can be discerned. Namely, for smaller angles of α , the ratio of l_1/l_2 is required to be higher for the optimal G.A.. This is caused by the fact that for larger angles the arm required to double the input displacement is more comparable to the input arm. As already discussed before, for $\alpha > 30$ the geometrical advantage criterion worsens. Furthermore, as long as $l > 20$ it does not seem to have a large influence on the behavior of the G.A..

Investigating Fig. S18 it is clear that as already earlier mentioned for the best sinusoidality a high α and l are needed. Furthermore, looking at the individual plots the performance regarding the sinusoidality seems opposite to that of the deviation of the G.A..

Examining Fig. S19, it becomes evident that for good load capacity a high angle of α accompanied by a small flexure length l is needed. This makes sense as lowering the butterfly flexures' length decreases their stiffness and thus increases the load capacity, and higher α is better as in this case the input and output load capacity are more evenly matched, such that the overall minimum of these two will be optimized. Furthermore, increasing the angle α , decreases the l_1/l_2 ratio needed. This can be intuitively understood by understanding that to have a good load capacity both the input and output capacity should be optimized simultaneously, to increase their minimum. The input and output capacity is dependent on the angle α as explained earlier, however, the ratio of l_1/l_2 also influences the load capacity by similarly changing the moment arm from the input or output to the butterfly flexures.

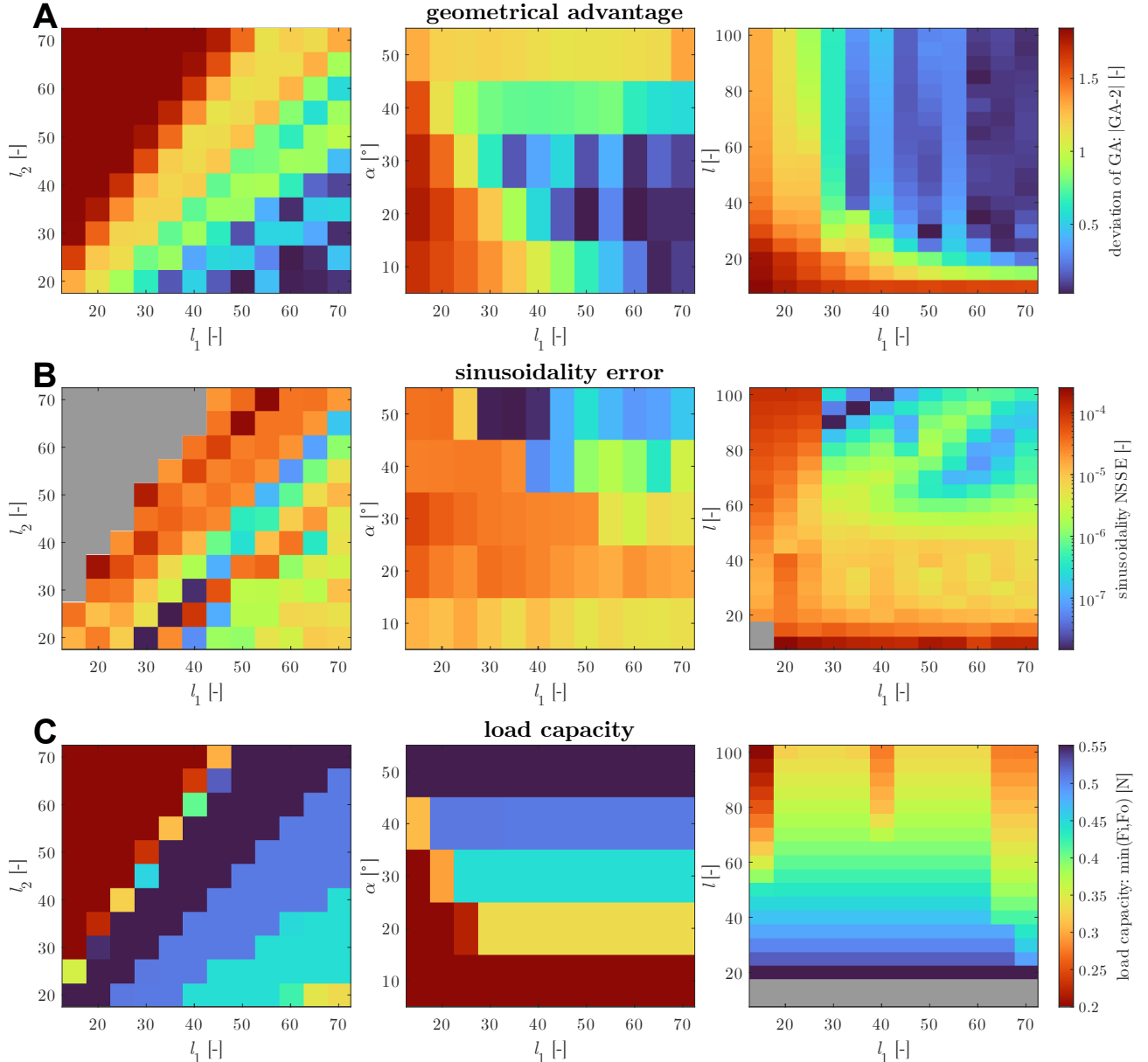


Fig. S16: Mechanical response of the frequency doubler regarding the criteria for the preliminary investigation. Evolution of, (A) the deviation of the geometrical advantage, $|(|G.A.) - 2|$, B, the sinusoidal normalized sum of square error, sinusoidal NSSE, and C the load capacity, $\min(F_o, F_i)$ as a function of the normalized horizontal distance between the butterfly flexures, l_1 and (left) the normalized vertical distance between the butterfly flexures, l_2 , (middle) the angle of the butterfly flexures α , and (right) the normalized butterfly flexure length, l .

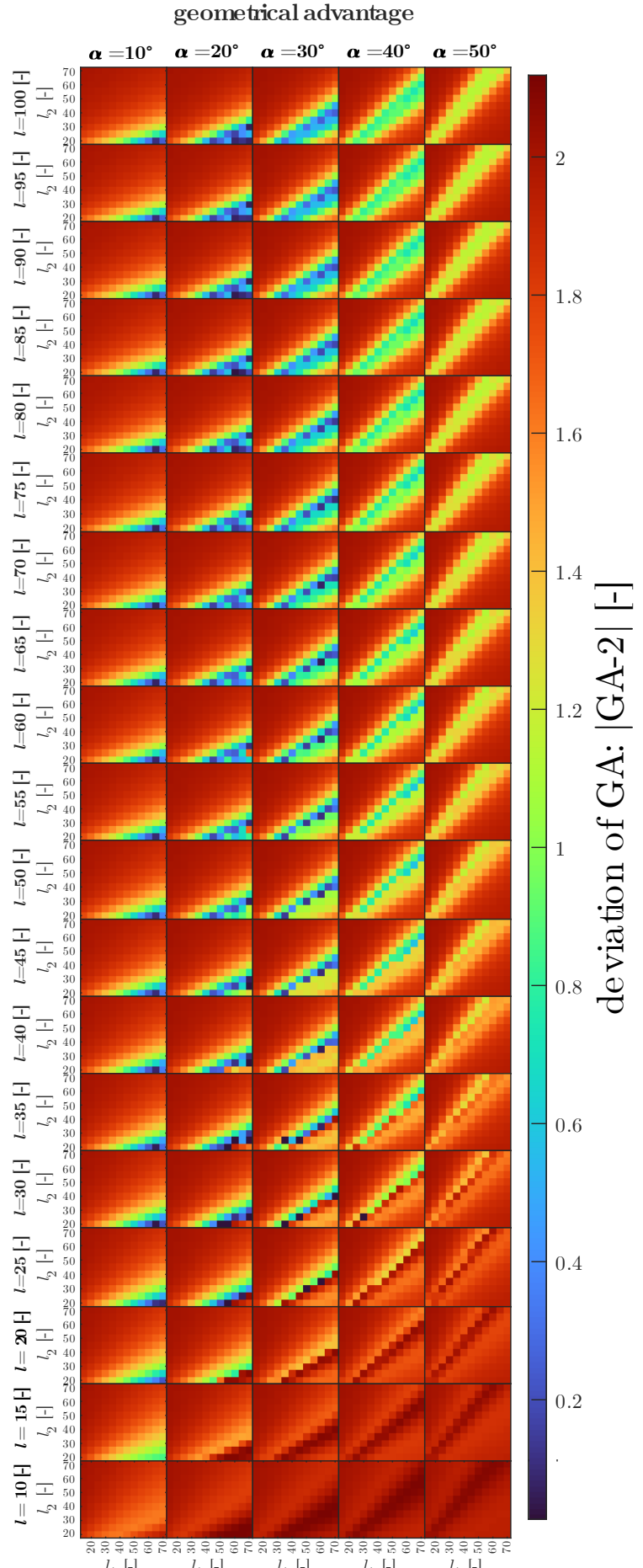


Fig. S17: Full mechanical response of the frequency doubler regarding the geometrical advantage for the preliminary investigation. Tiled plot layout for the normalized horizontal flexure distance (l_1) versus the normalized vertical flexure distance (l_2) versus the deviation in geometrical advantage, $|(G.A.) - 2|$. With a change in the angle of the butterfly flexures (α) versus the normalized length of the butterfly flexures (l) between plots.

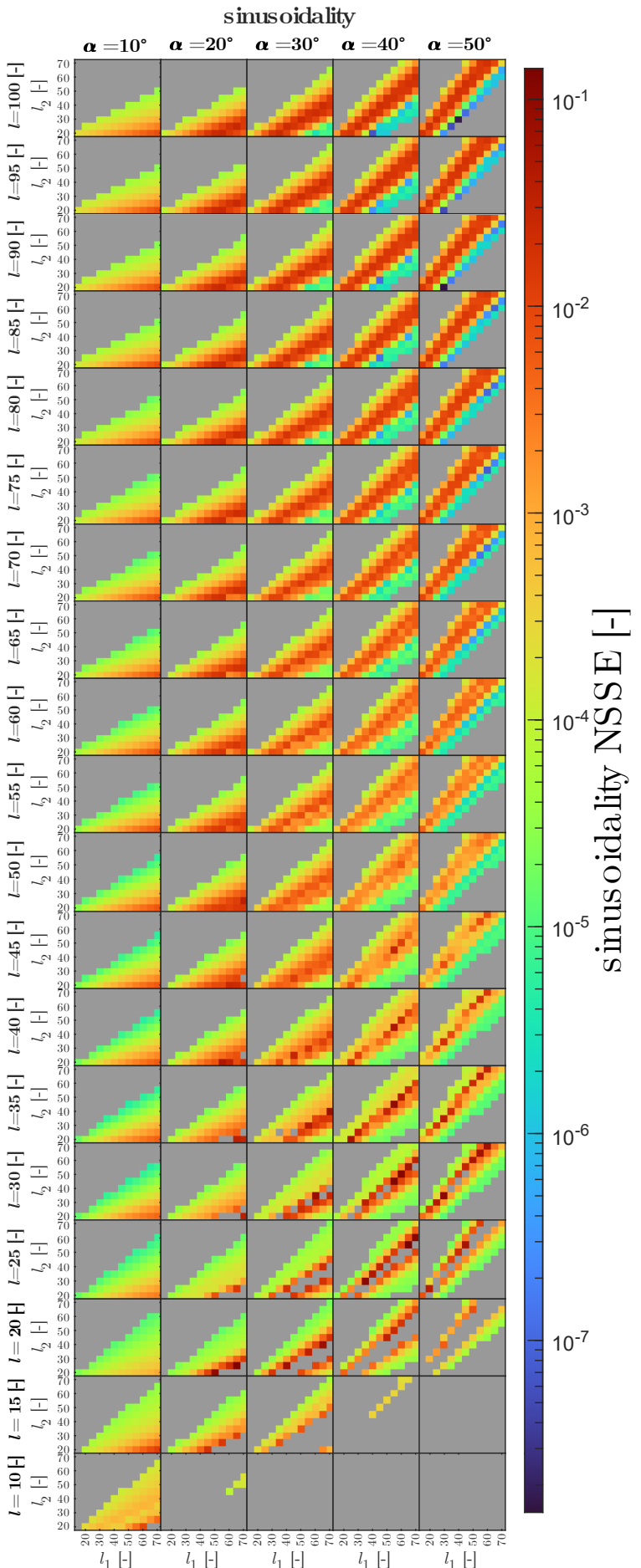


Fig. S18: Full mechanical response of the frequency doubler regarding the sinusoidality for the preliminary investigation. Tiled plot layout for the normalized horizontal flexure distance (l_1) versus the normalized vertical flexure distance (l_2) versus the sinusoidal normalized sum of square error, sinusoidality NSSE. With a change in the angle of the butterfly flexures (α) versus the length of the butterfly flexures (l) between plots.

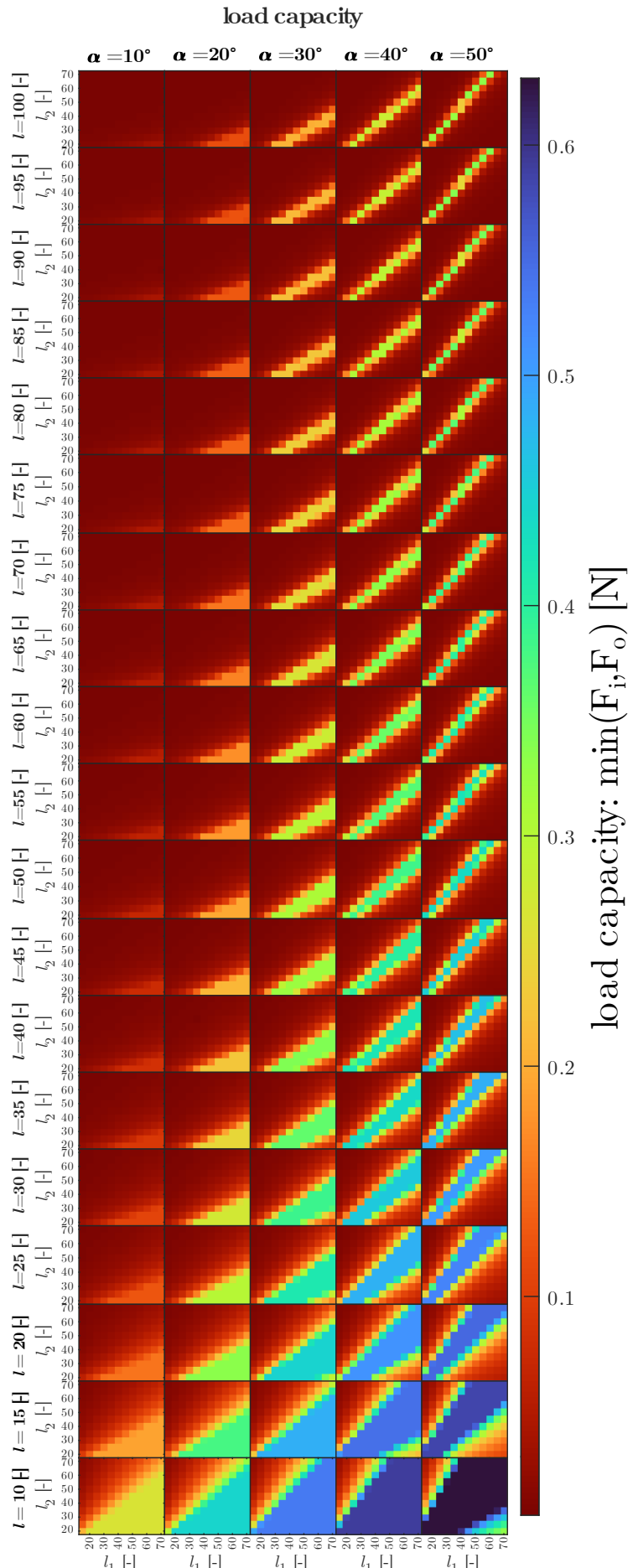


Fig. S19: Full mechanical response of the frequency doubler regarding the load capacity for the preliminary investigation. Tiled plot layout for the normalized horizontal flexure distance (l_1) versus the normalized vertical flexure distance (l_2) versus the load capacity, $\min(F_o, F_i)$. With a change in the angle of the butterfly flexures (α) versus the normalized length of the butterfly flexures (l) between plots.

B Complete scatter plots for all simulations showing criterion behavior

The scatter plots for multiple different criteria can be seen in Fig. S20. These plots were made in such a way that the best points regarding the geometrical advantage were plotted last such that they show up on top. Furthermore, the points where the deviation of the *G.A.* is less than a set constraint, $|G.A.| \leq 0.01$ are indicated with a black contour to highlight the behavior around these criteria for designs with a good geometrical response. Notice as well that in the case of load capacity, the criterion was only evaluated for the full preliminary investigation and designs fulfilling the hard constraint set on the *G.A.* during the iteration process.

From these plots, it becomes evident that a good *G.A.* can be found in certain areas which are encompassed by, $1.5 \leq L_1/L_2 \leq 3.5$, $\alpha < 35$, $S > 100$, $\text{sinusoidality} > 10 \times 10^{-3}$ and a load capacity $< 0.4 \text{ N}$. In the following discussion of the results, a large emphasis will be on the behavior of points within this area. Looking at the influence of the horizontal and vertical spacing (L_1/L_2) for good *G.A.* it can be observed that the influence on the sinusoidality is minimal as long as $L_1/L_2 \geq 1.5$. A similar thing can be seen for the angle α . This is caused by the fact that these two parameters are coupled such that a change in the angle only requires a different length ratio but does not immediately jeopardize the sinusoidality, as was also concluded from Fig. S17.

Observing the influence of the size on the sinusoidality and load capacity, it becomes evident that for a small deviation in the geometrical advantage, the sinusoidality improves for smaller sizes, similarly, the load capacity also generally improves for smaller sizes.

Examining the influence of the length ratio, L_1/L_2 , on the load capacity it is clear that a smaller ratio leads to an increase in the load capacity, however, this is ultimately limited by the *G.A.* around $L_1/L_2 > 1.5$. Furthermore increasing the angle α has a positive effect on the load capacity until it is limited at $\alpha < 35$ also by the geometrical advantage. As earlier discussed and can also be concluded from Fig. S19, the angle α and L_1/L_2 ratio are coupled for the load capacity. This expresses itself as an increase in α leads to a decrease in L_1/L_2 ratio required to optimize the load capacity, because of the moment arm from input-output and output-input changing for both the load capacity and the L_1/L_2 ratio.

C Concatenation of the best designs

In Fig. S21 the best designs found in the simulations are compared with the ideal sinusoidal for theoretical concatenation. Looking at the displacement ratio, the best designs only show a slight difference in behavior relative to each other, and as expected the best sinusoidal design corresponds the best to the ideal sinusoidal design. However, all three designs have small non-sinusoidalties which upon concatenation are amplified. The result of this is evident from the plots showing higher concatenation, where it can clearly be seen that the small deviation in GA and non-sinusoidality of the best load capacity get amplified each concatenation until a hugely non-sinusoidal behavior is shown after 5 concatenations. The non-sinusoidality shows itself in the fact that the designs have a changing frequency over the normalized cycle. While the deviation in the *G.A.* shows itself by exponentially growing each concatenation allowing a displacement outside of the expected range of 0-2 mm. Comparatively the sinusoidal mechanism as expected holds itself together the best for higher concatenations. Furthermore, when observing the force-displacement of the three designs, it becomes clear that the best sinusoidal mechanism does not show similar buckling behavior for the transition area as the best load capacity and best overall design do.

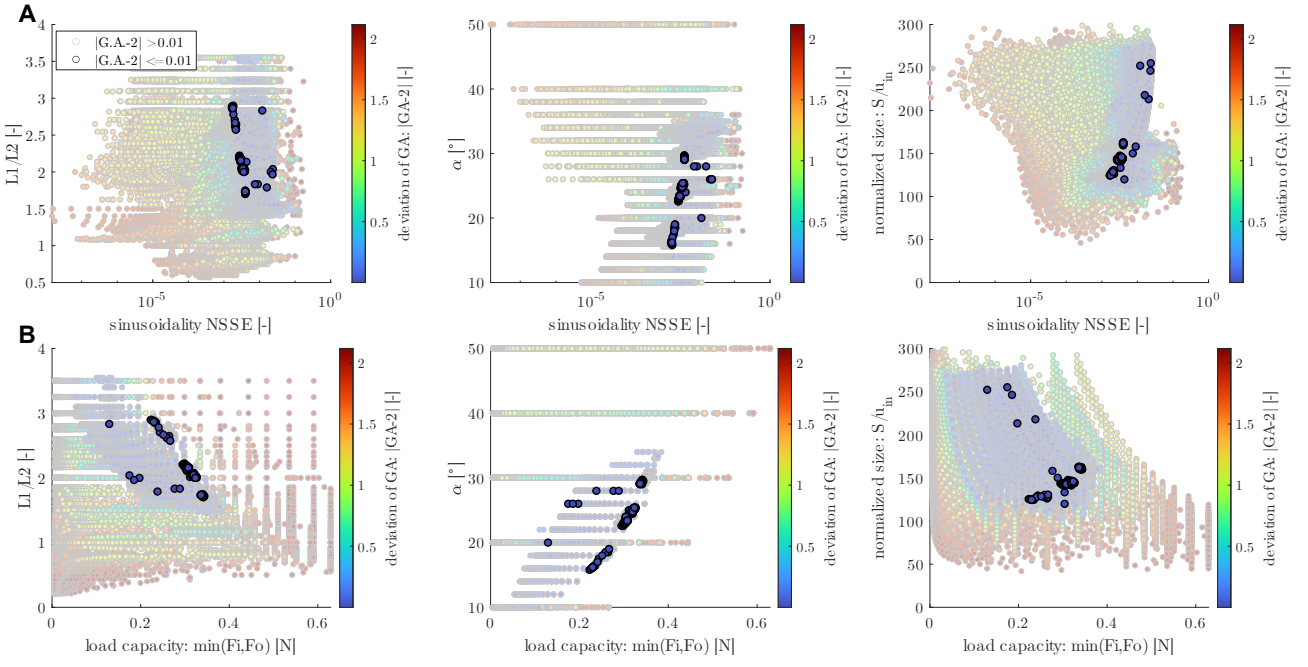


Fig. S 20: Scatter plots of all data for multiple different criteria. Scatter plots of, (A) sinusoidal normalized sum of square error, sinusoidal NSSE, or (B) load capacity, $\min(F_i, F_o)$ versus (left) the ratio of horizontal spacing over vertical spacing between the butterfly flexures, L_1/L_2 , (middle) the angle of the butterfly flexures with the horizontal (α), (right) the normalized size of the frequency doubler, S/u_{in} .

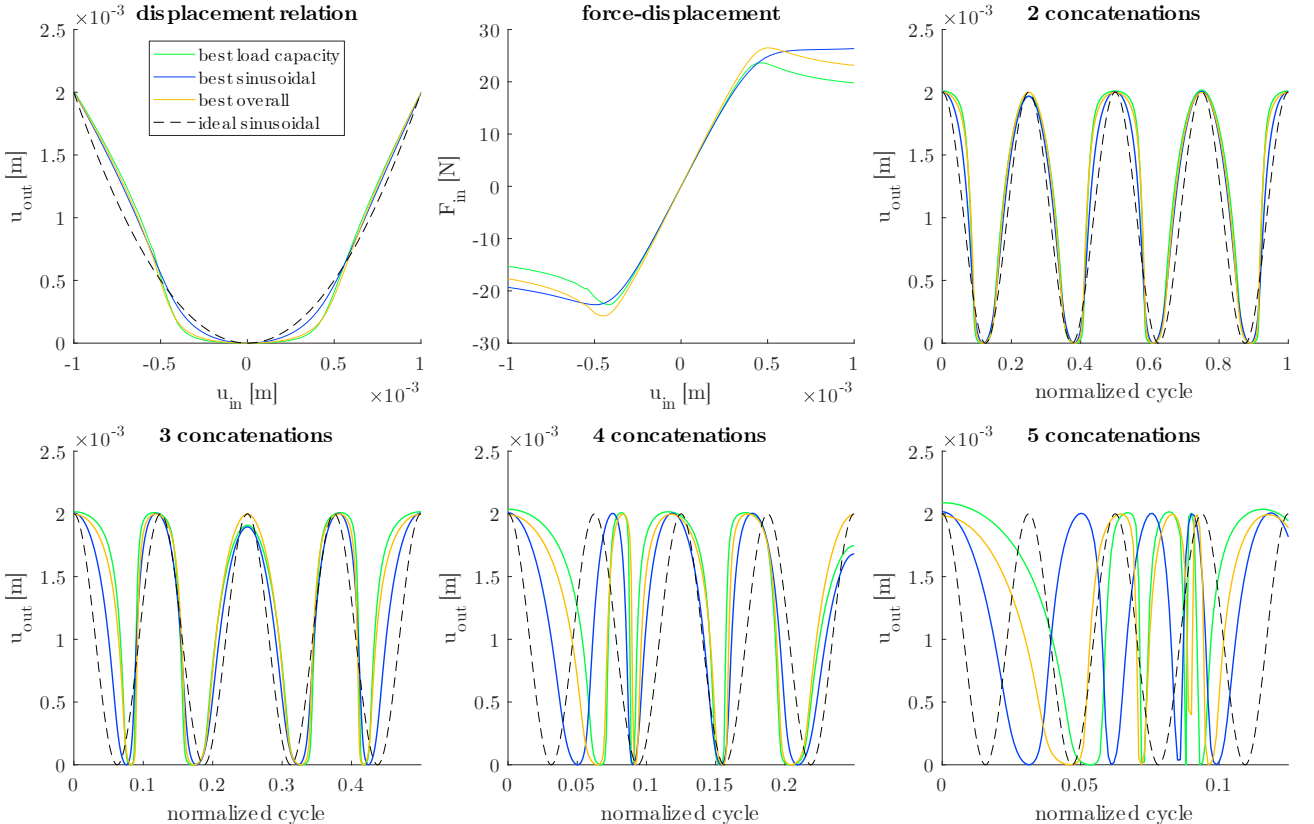


Fig. S 21: Displacement relation, force-displacement relation, and output upon theoretical concatenation of the best designs. Displacement relation, force-displacement relation and the output over the normalized cycle for 2,3,4 and 5 concatenations.

Section S6: Scripts

All scripts, data and other documents used to create this paper can be found in this GitHub:
<https://github.com/Luuk-Samuels/ThesisLuuk>

Movie S1. Displacement of the prototype during the experiment. Video showing the full displacement of the prototype during testing, starting at $u_{in} = 0$ mm, then consecutively moving the mechanism to $u_{in} = 3$ mm, $u_{in} = -3$ mm, and back to $u_{in} = 0$ mm. In the video the back view of the mechanism showing the displacement of the output is shown.

Movie S2. Displacement of the FEM simulation. Back view of the simplified mechanism in Ansys showing the displacement from $u_{in} = 3$ mm to $u_{in} = -3$ mm, while simultaneously indicating the von-Mises stress in the mechanism.

Movie S3. Displacement of the non-rigid FEM simulation. Back view of the full manufactured mechanism in Ansys showing the displacement from $u_{in} = 3$ mm to $u_{in} = -3$ mm, while simultaneously indicating the von-Mises stress in the mechanism.